Article

Disentangling Random Motion and Flow in a Complex Medium

Elena F. Koslover,[1] Caleb K. Chan,[1] and Julie A. Theriot[1,2,3,*]
[1]Department of Biochemistry, [2]Department of Microbiology and Immunology, and [3]Howard Hughes Medical Institute, Stanford University School of Medicine, Stanford, California

ABSTRACT We describe a technique for deconvolving the stochastic motion of particles from large-scale fluid flow in a dynamic environment such as that found in living cells. The method leverages the separation of timescales to subtract out the persistent component of motion from single-particle trajectories. The mean-squared displacement of the resulting trajectories is rescaled so as to enable robust extraction of the diffusion coefficient and subdiffusive scaling exponent of the stochastic motion. We demonstrate the applicability of the method for characterizing both diffusive and fractional Brownian motion overlaid by flow and analytically calculate the accuracy of the method in different parameter regimes. This technique is employed to analyze the motion of lysosomes in motile neutrophil-like cells, showing that the cytoplasm of these cells behaves as a viscous fluid at the timescales examined.

INTRODUCTION

Single-particle tracking has become a widespread method for studying the microrheology of complex fluids, including mucus (1), active gels (2), and the interior of living cells (3,4). In the latter case, the motion of tracer particles provides valuable information about material properties and active fluctuations in the cytoplasm, as well as how these properties vary with cytoskeletal structure (5), metabolic activity (6,7), differentiation state (8), and metastatic potential (9).

A common approach to analyzing particle trajectories is to calculate the mean-squared displacement (MSD) of the particles over different time intervals, averaged over time and ensemble of particles. The shape of the MSD curve depends on the material properties of the medium and the time correlation of forces acting upon the particles. For particles subjected to thermal forces in a purely viscous medium, the MSD scales linearly with time as MSD $\sim t$. In a viscoelastic medium, thermally driven particles exhibit fractional Brownian motion with subdiffusive scaling, MSD $\sim t^{\alpha}$, where $\alpha < 1$ (10). In the presence of persistent forces or flows in the medium, the MSD exhibits a superdiffusive component, with a ballistic scaling (MSD $\sim t^2$) for constant flows. For long times, strong flows, or large (slowly diffusing) particles, the ballistic motion dominates over the thermal motion of the particle, obscuring the high-frequency component that carries information about the material properties of the medium.

In the context of a complex dynamic environment, such as the interior of a living cell, the stochastic motion of particles is determined by a combination of thermal and actively generated forces as well as the frictional resistance of the medium. Although the relative contribution and time variation of the active forces remains a matter of debate (6,11,12), it is acknowledged that studying passive particle motion in a cell yields valuable insight regarding the intracellular physical environment. To quantify such stochastic motion, however, it is necessary first to disentangle it from the bulk, slowly varying flows that can occur in many cell types.

In this work, we present a technique for analyzing the high-frequency stochastic motion of particles under thermal (or similarly correlated) forces in the presence of spatially heterogeneous underlying flow of the medium. Our method, termed BNEW (Brownian noise extracted with wavelets), relies on wavelet analysis (13) to subtract out slowly varying components of the motion from individual particle trajectories. Appropriate rescaling of the remaining data allows for accurate extraction of a diffusion coefficient and scaling exponent, α, even in the presence of significant and complex flow.

As an example application, we study the stochastic motion of lysosomes within the cytoplasm of motile HL60 neutrophil-like cells. Although previous single-particle tracking studies have demonstrated a viscous cytoplasm in some stationary cell types (8,14) and a viscoelastic one in others (15–17), the microscopic material properties within such rapidly moving cells remain uncharacterized. HL60 cells crawl on a two-dimensional surface, with significant changes in shape engendering internal flow and deformation of the cytoplasmic contents. This flow of the cytoplasmic medium precludes use of the usual approach to extracting microrheological information from single-particle tracks, but makes this system an ideal candidate for the BNEW method. We use this technique to demonstrate that organelle motion in HL60 cells is consistent with motion through a

Submitted August 20, 2015, and accepted for publication November 5, 2015.

*Correspondence: theriot@stanford.edu

Editor: Douglas Robinson.

0006-3495/16/02/0700/10

http://dx.doi.org/10.1016/j.bpj.2015.11.008

viscous cytoplasm, with an effective viscosity ~50 times that of water, over the timescales examined (>50 ms).

MATERIALS AND METHODS

Culturing of HL60 cells

Neutrophil-like HL60 cells were maintained in RPMI media (22400, Invitrogen, Carlsbad, CA), supplemented with 10% fetal bovine serum (FBS) (Gemini, Elizabeth, NJ) and antibiotic-antimycotic drugs (15240, Gibco, Grand Island, NY). The cultured cells were incubated at 37°C in 5% CO_2 and passaged once every 2–3 days to a density of 2×10^5 cells/mL. To differentiate the HL60 cells, cells were diluted in RPMI full media containing 1.3% dimethylsulfoxide (61097, Acros, Morris Plains, NJ) with an initial density of 2×10^5 cells/mL. For all experiments, only cells differentiated for 5–6 days were used.

Lysosome labeling in HL60 cells

Before the agarose gel preparation step for the two-dimensional (2D) cell migration assay, about 10^5 differentiated HL60 cells were spun down at $500 \times g$ for 5–10 min and resuspended in 1 mL of L-15 media (21083-027, Gibco). Stock 1m M LysoTracker Deep Red (L12492, Molecular Probes, Eugene, OR) was diluted 1:10 to 100 μM in dimethylsulfoxide, and 1 μL of this 1:10 labeling solution was added to the L-15 cell suspension to reach a final concentration of 100 nM. The label-containing cell suspension was then incubated at 37°C for 30 min before being repelleted at $500 \times g$ for 5–10 min and resuspended in 1 mL of L-15 in preparation for being used in the under-agarose assay.

Under-agarose 2D cell migration assay

In this assay, differentiated HL60 cells were confined to migrate in a quasi-2D environment between an agarose pad and a fibronectin-coated coverslip. To cast the agarose pad, we first prepared a 2% low-melting-point agarose solution (16520, Invitrogen) by dissolving the agarose powder in heated L-15 media, and the solution was kept in a 37°C waterbath until use (solution A). We then prepared a 2× stock solution of L-15 media (21083-027, Gibco) with 20% FBS (solution B). f-MLP (F3506, Sigma-Aldrich, St. Louis, MO) was added as a chemoattractant to solution B at a final concentration of 2 nM to induce chemokinesis. Solutions A and B were then mixed at a 1:1 ratio and pipetted immediately to a mold to cast the agarose pad. The agarose was kept at room temperature for at least 20 min to solidify. For regular time-lapse imaging, we used agarose pads with a minimal thickness of ~2 mm.

The LysoTracker-labeled cell suspension was spun down at $500 \times g$ for 5–10 min, and then concentrated to a final volume of 10 μL by removing the supernatant (cell concentration = 10^4 cells/μL). The concentrated cell solution was then added to the center of a coverslip that was precoated with 10 μg/mL fibronectin (F2006, Sigma-Aldrich). The solidified agarose pad was overlaid above the 10 μL cell solution. The gel-covered coverslip was transferred to a microscope adaptor and then used for time-lapse imaging. Typically, the agarose pad would start compressing the cells within 20 min. After the cells were fully confined under the pad, the apparent cell area would increase, and the brightness of the phase halo around the cell would decrease in phase-contrast images. Imaging was initiated only after the cells were fully confined under this definition. The ambient temperature was maintained at 37°C with a temperature-controlled chamber (Haisen Tech, Guangdong, China).

Fixation of LysoTracker-labeled HL60 cells

LysoTracker-labeled HL60 cells undergoing 2D chemokinesis were fixed and used as a control for localization error calculations (Section S10 in the Supporting Material). Differentiated HL60 cells were labeled with LysoTracker and prepared for the under-agarose 2D migration assay. After the cells were fully confined, cell migration was allowed to continue under agarose for 5 min before 1 mL of cytoskeleton buffer (CSK: 100 mM HEPES, pH 7.0, 138 mM KCl, 3 mM $MgCl_2$, 2 mM EGTA, and 320 mM sucrose), containing 3.7% formaldehyde and 0.05% glutaraldehyde, was added directly on top of the agarose pad, followed by a fixation period of 20 min. The CSK buffer was then aspirated and replaced with 1× phosphate-buffered saline, and the cells were imaged under the same settings as the under-agarose 2D cell migration assay.

Microscopy

To capture intracellular lysosome motion with high spatiotemporal resolution, time-lapse images were acquired using a Nikon Eclipse Ti epifluorescent microscope with a 100× oil-immersion objective and a 5.5 megapixel high-speed, high-sensitivity sCMOS camera, the Andor Zyla 5.5 (Andor, Belfast, United Kingdom). Acquisition rate was set to 20 frames/s (exposure time = 50 ms) with a region of interest of 1392 × 1040 pixels. A temperature and humidity control unit (Haisen Tech) was installed with the microscope to maintain a constant temperature of 37°C during the entire imaging session.

Periodic overlaying of the phase-contrast and fluorescent channels in some of the image stacks (see, e.g., Fig. 4 *a*) was achieved by programming an Arduino Uno microcontroller board (Arduino, Somerville, MA) as hardware interface between the Andor Zyla camera and the T-Cube LED driver (Thorlabs, Newton, NJ), which controlled the transmitted LED light source. During the imaging of fluorescently labeled lysosomes, the Arduino board would track the number of exposures made and turn on the LED light source for a specific duration after a predetermined number of exposures. Both the LED-on duration and the interval between consecutive LED-on sessions were programmable from the Arduino board.

A stage micrometer was used to determine the conversion factor of 1 pixel (px) = 0.13 μm.

Image processing

Approximate contours of individual cells were segmented from each image using Otsu thresholding, with the thresholding level scaled down by a factor of 0.3–0.5, as manually determined for each image stack to achieve accurate segmentation based on background fluorescence. Segmentation was carried out every 20 frames (1 s intervals), with spline interpolation of the cell contour for the intervening images. For several of the videos, intermittent phase-contrast images were taken every 200 frames (10 s intervals) to obtain a more accurate approximation of the cell contour (see Fig. 4, *a* and *b*). Phase images were segmented using the directional gradient vector flow algorithm (18), with manual adjustment near the lamellipod region.

Within the segmented regions (dilated by 50 px on all sides), individual lysosomes were identified by standard particle tracking algorithms as described by Crocker and Grier (19). Publicly available code (20) was used to apply a bandpass filter (with cutoffs at 1 px and 8 px (1 μm)), identify local maxima, and pick out centroids of intensity peaks. Identified features were filtered to retain only those with an eccentricity <0.3, a maximal intensity in the top 10% of the image values, an intensity per pixel above 30% of the maximal image intensity, and a total intensity above the 80th percentile (for squared regions of size 8 × 8 px).

Linking of features into particle trajectories was carried out using the same software package (20). To further remove artifacts, only trajectories of at least 40 time steps were retained for further analysis. A maximal step size of 6 px (0.77 μm) was imposed, and trajectories were split at all missed frames. Only those cells with at least 100 particle trajectories were used for the BNEW analysis. Of 120 imaged cells, 93 cells satisfied this criterion and were included in the analysis.

Trajectories were thresholded to remove the most rapidly moving particles (generally corresponding to regions of unusually high flow), using a

wavelet-based method previously described for identifying actively transported organelles (21). Smoothed local velocities were defined using third-order Savitsky-Golay wavelets with a span of $n = 20$ (see Section S2). For each cell, the threshold for locally smoothed velocity magnitude was set at twice the standard deviation for all particles within that cell. Trajectories were broken up whenever a particle exceeded the smoothed velocity threshold, with on average 8% of the total trajectory length for each cell falling above the threshold.

The cell frame of reference (see Fig. 4, *c* and *d*) was found by cross-correlating rectangular regions surrounding each cell between every 10th frame of the fluorescent images (time intervals of 0.5 s).

RESULTS

Extracting Brownian motion with wavelet analysis

We describe the BNEW technique for analyzing particle trajectories composed of stochastic Brownian (or fractional Brownian) motion overlaid on slowly varying drift. This method relies on leveraging the separation of velocity correlation timescales to characterize the scaling and diffusion coefficient associated with the high-frequency stochastic component of the motion. Standard methods for dedrifting particle trajectories rely on averages of many particles, all assumed to be undergoing the same drift (22). The BNEW method makes no such assumption, since it relies on correcting for the flow in each individual trajectory before recompiling the data to quantify the collective statistics of the stochastic motion. This method is thus ideal for the analysis of stochastic motion in the presence of complex, spatially inhomogeneous flows (e.g., Fig. 1 *a*).

Specifically, we consider the motion of particles with 2D trajectories given by

$$\vec{p}_k - \vec{p}_0 = \Delta \sum_{i=0}^{k-1} (\vec{u}_i + \vec{v}_i) + \vec{\xi}_k - \vec{\xi}_0, \tag{1}$$

where $\vec{p}_k$ is the position of the particle at time step k, Δ is the size of the time step, $\vec{u}_i$ is the drift velocity at time step i, $\vec{v}_i$ is the velocity associated with Brownian motion, and ξ_k is the localization error. We begin by assuming that the stochastic

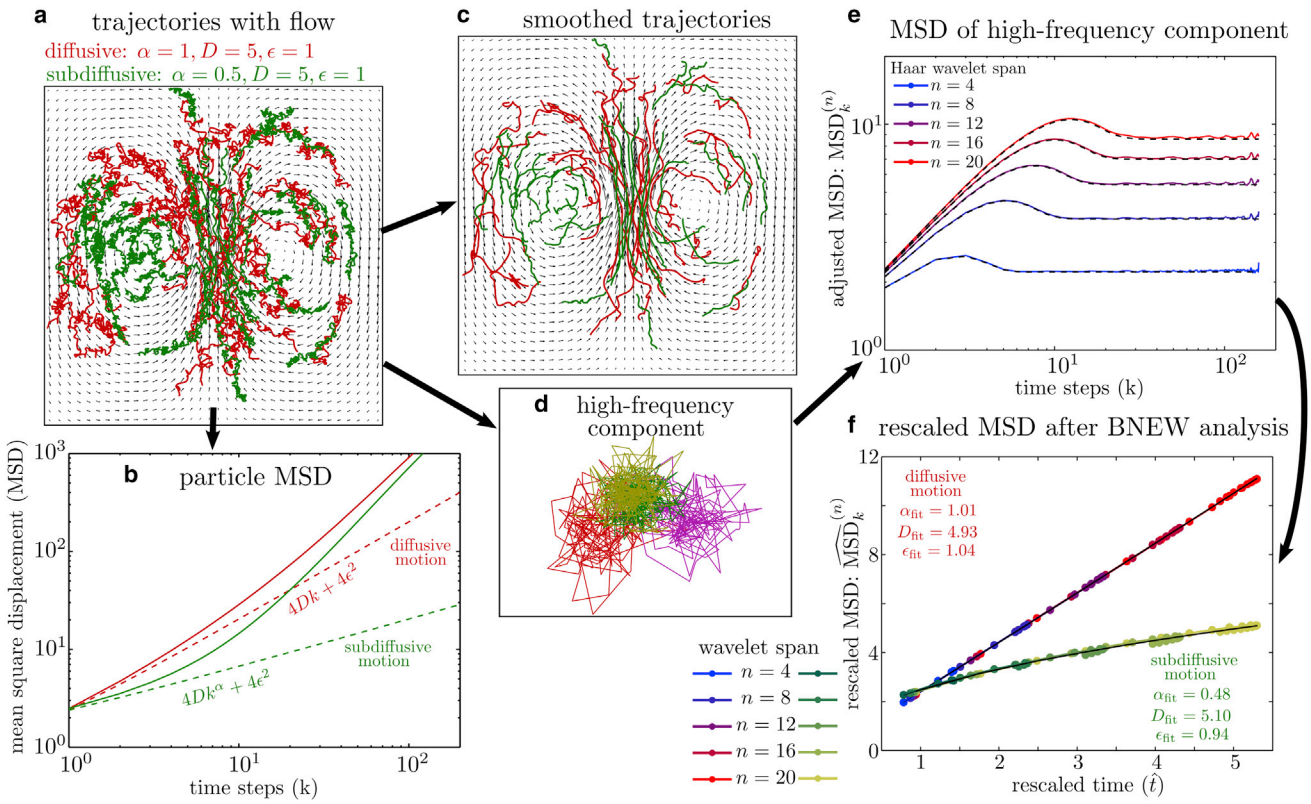

FIGURE 1 Schematic of the BNEW method for decoupling high-frequency stochastic motion from flow, as applied to simulated particle trajectories. (*a*) Particles undergoing diffusive Brownian motion (*red*, $\alpha = 1, D = 5$) and subdiffusive, fractional Brownian motion (*green*, $\alpha = 0.5, D = 5$) were simulated in the presence of a flow field (*black arrows*), with localization error $\epsilon = 1$. Example trajectories are shown (from 400 total trajectories of length 200 time steps each). (*b*) The MSD for simulated particles. Superlinear scaling is a result of the underlying flow. Dashed lines indicate the MSD with no drift present for diffusive (*red*) and subdiffusive (*green*) motion. (*c* and *d*) Decomposition of the particle trajectories into the smoothed component (*c*) and the high-frequency component, $\vec{p}_k^{(n)}$ (*d*). Two high-frequency trajectories are shown for diffusive (*red* and *magenta*) and subdiffusive (*green* and *yellow*) motion. Smoothing was done using Haar wavelets with span $n = 12$. (*e*) Adjusted MSD obtained with BNEW analysis for tracks with diffusive stochastic motion. Dashed black lines show the analytical solution (Eq. 9). (*f*) Rescaled adjusted MSD, as defined in Eq. 11, plotted on linear axes. Black lines indicate power-law fits to the data, with the given fit parameters. To see this figure in color, go online.

velocities, $\vec{v}_i$, are characteristic of diffusive Brownian motion and are thus independent and normally distributed, with mean 0 and variance $2D\Delta$ in each dimension. Similarly, the localization errors, ξ_k, are assumed to be independently normally distributed with mean 0 and variance ϵ^2 in each dimension. In the absence of drift, the MSD of the particle trajectories is given by

$$\left\langle |\vec{p}_k - \vec{p}_0|^2 \right\rangle = 4Dt^\alpha + 4\epsilon^2, \tag{2}$$

with the scaling exponent $\alpha = 1$ under the assumption of uncorrelated stochastic velocities.

On timescales over which it remains approximately constant, the drift velocity, $\vec{u}$, will contribute a ballistic term ($\sim t^2$) to the total MSD. If the magnitude of the drift is large enough, this term will dominate over diffusion, making it impractical to characterize the diffusive component of the motion by the usual linear fitting of the MSD curve (Fig. 1 *b*). The goal of the method described here is to obtain an estimate of the scaling, α, the diffusion coefficient, D, and the localization error, ϵ, from such trajectories, by correcting for the drift velocity, $\vec{u}$.

A common signal-processing technique for extracting approximate velocities from noisy data is that of wavelet analysis (13,21). This procedure involves taking a sliding window over each trajectory and using a linear combination of data points within that window to approximate the velocity of the particle:

$$\vec{v}_i^{\,w} = \sum_{j=-n}^{n} w_j \vec{p}_{i+j}, \tag{3}$$

where $2n+1$ is the window size. A number of different wavelet shapes, $\{w_j\}$, can be used for this purpose, and the procedure is equivalent to smoothing the data or applying a low-pass filter.

To provide a meaningful local velocity estimate, the wavelet coefficients must satisfy the constraints

$$\sum_{j=-n}^{n} w_j = 0 \quad \text{and} \quad \sum_{j=-n}^{n} j w_j = 1. \tag{4}$$

The commonly used Haar wavelet for velocity approximation (Section S1) and the Savitsky-Golay wavelets often used for data smoothing and differentiation (Section S2) all share these properties. Different wavelet shapes smooth the data to a different extent for a given span and involve more or less sharp cutoffs between the low-frequency passband and the high-frequency stopband when viewed as low-pass filters (23).

To characterize the high-frequency stochastic motion of the particle, we subtract out the smoothed curve resulting from the wavelet analysis and focus on the adjusted tracks, $[\vec{p}_k^{\,(n)} = \vec{p}_k - \sum_{i=0}^{k-1} \vec{v}_i^{\,w}]$, that remain (Fig. 1, *c* and *d*). If the drift velocity remains approximately constant over the span of the wavelet, then the contribution of the drift to the particle motion is effectively removed by this procedure.

Any wavelet that satisfies the constraints in Eq. 4 can be equivalently defined by a set of coefficients associated with trajectory steps between consecutive time points ($\vec{s}_i = \vec{p}_{i+1} - \vec{p}_i$). That is, we can find coefficients $\widehat{w}_j$ such that, for any trajectory, the velocity approximation at point i is given by

$$\vec{v}_i^{\,w} = \sum_{j=-n}^{n} w_j \vec{p}_{i+j} = \sum_{j=-n}^{n-1} \widehat{w}_j \vec{s}_{i+j}. \tag{5}$$

Specifically, the coefficients $\widehat{w}_j = -\sum_{l=-n}^{j} w_l$ satisfy this property. Furthermore, the second constraint in Eq. 4 ensures that $\sum_{j=-n}^{n-1} \widehat{w}_j = 1$.

The adjusted trajectories after subtracting out the smoothed motion from the wavelet analysis are then given by

$$\begin{aligned} \vec{p}_k^{\,(n)} - \vec{p}_0^{\,(n)} &= \sum_{i=0}^{k-1} \left(\vec{s}_i - \vec{v}_i^{\,w}\right) \\ &= \sum_{i=0}^{k-1} \left[\vec{s}_i - \sum_{j=-n}^{n-1} \widehat{w}_j \vec{s}_{i+j}\right] = \sum_{i=-n}^{k+n-2} \widehat{c}_i \vec{s}_i \\ &= \Delta \sum_{i=-n}^{k+n-2} \widehat{c}_i (\vec{u}_i + \vec{v}_i) + \sum_{i=-n}^{k+n-1} c_i \vec{\xi}_i, \end{aligned} \tag{6}$$

where

$$\widehat{c}_i = h_i - \sum_{j=\max(-n,i-k+1)}^{\min(n-1,i)} \widehat{w}_j, \tag{7}$$

$$\begin{aligned} h_i &= \begin{cases} 1 & \text{for } 0 \le i < k \\ 0 & \text{otherwise} \end{cases}, \\ c_i &= \begin{cases} -\widehat{c}_i, & \text{for } i = -n \\ \widehat{c}_{i-1} - \widehat{c}_i, & \text{for } -n < i \le k+n-2 \\ \widehat{c}_{i-1}, & \text{for } i = k+n-1 \end{cases}. \end{aligned} \tag{8}$$

As a sum of independent, normally distributed random variables, the adjusted trajectory points are also normally distributed. If we assume that the drift velocity is constant ($\vec{u}_i = \vec{u}$), then the mean of $\vec{p}_k^{\,(n)} - \vec{p}_k^{\,(n)}$ vanishes due to the constraints on the wavelet coefficients (Eq. 4). The MSD of the adjusted trajectories is given by

$$\mathrm{MSD}_k^{(n)} = \left\langle \left| \vec{p}_k^{\,(n)} - \vec{p}_0^{\,(n)} \right|^2 \right\rangle = 4D\Delta A_k^{(n)} + 4\epsilon^2 B_k^{(n)}, \tag{9}$$

where the average is over both time and ensemble of particles and the functions

$$A_k^{(n)} = \sum_{i=-n}^{k+n-2} \widehat{c}_i^{\,2}, \quad B_k^{(n)} = \frac{1}{2} \sum_{i=-n}^{k+n-1} c_i^2 \tag{10}$$

are fully determined by the shape and span of the wavelet used. For the commonly employed Haar wavelet (13), these functions are calculated in closed form (Section S1). More complicated wavelet shapes can be handled by performing the summations in Eqs. 7, 8, and 10 numerically (implemented in the Supporting Material). The adjusted MSD (Eq. 9) is plotted together with simulated data in Fig. 1 *e*. The $\mathrm{MSD}_k^{(n)}$ increases for short times, but flattens out for times $>2n$, since the smoothed track cannot deviate far from the original data.

Although the span, n, of the wavelet has a large effect on the adjusted MSD curves, these curves can be rescaled using Eq. 9 to give

$$\widehat{\mathrm{MSD}}_k^{(n)} = 4D\Delta\hat{t}_k + 4\epsilon^2, \tag{11}$$

where $\widehat{\mathrm{MSD}}_k^{(n)} = \mathrm{MSD}_k^{(n)}/B_k^{(n)}$ and $\hat{t}_k = A_k^{(n)}/B_k^{(n)}$ is a rescaled dimensionless time. This transformation results in curves from all different wavelet spans collapsing onto a single universal line (Fig. 1 *f*). The diffusion coefficient and localization error can then be obtained by a linear regression of the data processed with several different wavelet spans $(2 \le n \le n_{\max})$. To avoid edge effects, the first and last $n_{\max}$ data points of each track are excluded from the calculation of the rescaled adjusted MSD.

We note that one of the fundamental strengths of the BNEW method is that each particle trajectory is analyzed independently, with the underlying flow approximated separately for each particle. In principle, this method can thus be applied for quantifying the high-frequency motion of individual particles. In practice, however, subtracting out the smoothed particle motion necessarily discards data on long-time particle behavior. The regression results are then much more sensitive to the noise inherent in finite sampling. Thus, obtaining an accurate characterization of the particle motion requires either recording very long trajectories or performing an ensemble average over many trajectories (as is the case for all results shown here). This ensemble average, however, can be performed over particles embedded in a spatially heterogeneous flow.

Characterizing subdiffusive motion

We next turn our attention to the case where the stochastic motion is subdiffusive. Subdiffusion can arise in a number of situations, including confinement, transient binding events, or motion in a viscoelastic medium (24). Here, we focus on the latter case, which has been shown to be applicable to the bacterial (4) and eukaryotic (16,17,25) cytoplasm, as well as the eukaryotic nucleoplasm (26). Particles in a viscoelastic medium undergo fractional Brownian motion, with negative velocity correlations that decay as a power law in time $[\langle \vec{v}(t)\cdot\vec{v}(t+\tau)\rangle = 2D\alpha(\alpha-1)|\tau|^{\alpha-2}]$ (10). The MSD associated with such motion is given by $\mathrm{MSD} = 4Dt^\alpha$, and we refer to the scaling exponent, α, as the viscoelastic scaling throughout this work. The limiting case of $\alpha \to 1$ recovers classical diffusive motion.

We show that the BNEW method can also be applied to trajectories with fractional Brownian motion overlaid on an approximately constant drift (Section S3). In this case, the rescaled $\widehat{\mathrm{MSD}}_k^{(n)}$ collapses on an approximate power-law curve for all wavelet spans and for time separations, k, that are small relative to span n (Fig. 1 *d*). We fit the rescaled MSD as a function of rescaled time, $\hat{t}$, to the power law:

$$\begin{aligned} \widehat{\mathrm{MSD}}_k^{(n)} &= 4\widehat{D}\Delta^\alpha \hat{t}_k^\alpha + 4\widehat{\epsilon}^2 \\ \widehat{D} &= Df(\alpha) \\ \widehat{\epsilon}^2 &= \epsilon^2 + D\Delta^\alpha g(\alpha)^2, \end{aligned} \tag{12}$$

where α, $\widehat{D}$, and $\widehat{\epsilon}$ are the fitted parameters. The functions $f(\alpha)$ and $g(\alpha)$ depend on the wavelet shape, as well as the range of time separations, k, used for fitting (Section S3). By fitting to this functional form, we can extract the characteristic exponent α of the fractional Brownian motion, as well as the effective diffusion coefficient, D, and localization error, ϵ. The BNEW method thus permits a characterization of the underlying medium as viscous or viscoelastic while correcting for the presence of flow.

Validation with nonconstant drift

The BNEW method provides an accurate characterization of stochastic motion in the case where the drift velocity is approximately constant over the time span of the wavelet. Before applying it to real data, however, it is important to validate this approach in the presence of time-varying drift. For concreteness, we consider the case where the drift velocity, $\vec{u}_i$, can be described as a 2D persistent random walk, characterized by correlation time τ and magnitude γ (Section S4). Such a random walk has an exponentially decaying velocity correlation; more complicated motion with several characteristic correlation times may be approximated as a sum over multiple persistent random walks (Section S9). We calculate the accuracy of the parameters α_{fit}, D_{fit}, and ϵ_{fit}, as obtained by fitting the rescaled MSD curve to a power law (Section S5). In particular, we consider the relative bias in the parameters, defined as $\langle \chi_{\mathrm{fit}} - \chi\rangle/\chi$ and the root mean-squared error, defined as $\sqrt{\langle(\chi_{\mathrm{fit}}-\chi)^2\rangle}/\chi$, where χ is each of the fitted parameters. Here, we focus on the case of purely diffusive stochastic motion $(\alpha = 1)$.

To simplify the parameter space, we nondimensionalize all time units by the time step, Δ, and all length units by the localization error, ϵ, leaving three dimensionless parameters: drift magnitude, $\tilde{\gamma} = \gamma\Delta/\epsilon$, drift correlation time, $\tilde{\tau} = \tau/\Delta$, and diffusion coefficient, $\tilde{D} = D\Delta/\epsilon^2$. The time-varying drift velocity is not fully removed by the BNEW procedure and leads to a bias in the estimation of α and D (Fig. 2, *a* and *b*). This effect is more pronounced when using

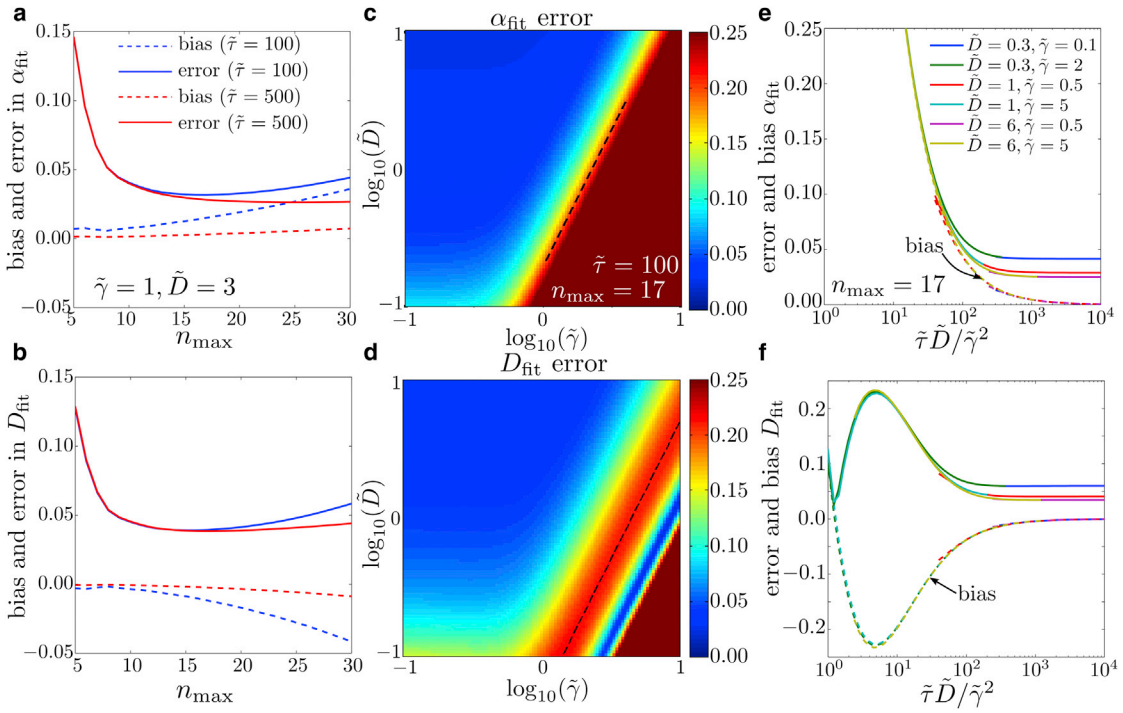

FIGURE 2 Errors in characterizing high-frequency stochastic motion with the BNEW method. (*a*) Bias and total error in the fitted scaling parameter, $\alpha_{\rm fit}$, as a function of maximal wavelet span. Dashed curves give the relative bias, $[\langle\alpha_{\rm fit} - \alpha\rangle/\alpha]$, and solid curves the relative error $[\sqrt{\langle(\alpha_{\rm fit} - \alpha)^2\rangle}/\alpha]$, calculated as described in Section S5, for drift correlation times of 100 time steps (*blue*) and 500 time steps (*red*). Curves shown are calculated for $\widetilde{\gamma} = 1, \widetilde{D} = 3$. (*b*) Corresponding curves for bias and error in $D_{\rm fit}$. (*c* and *d*) Dependence of relative error in $\alpha_{\rm fit}$ and $D_{\rm fit}$ on dimensionless drift magnitude, $\widetilde{\gamma}$, and diffusion constant, $\widetilde{D}$. All values are calculated with $\widetilde{\tau} = 100$ and $n_{\rm max} = 17$. Dashed black lines mark a constant value of $\widetilde{D}/\widetilde{\gamma}^2$. (*e* and *f*) Relative bias (*dashed curves*) and error (*solid curves*) plotted as a function of the compound parameter, $\widetilde{\tau}\widetilde{D}/\widetilde{\gamma}^2$. Persistence-time values of $10 \leq \widetilde{\tau} \leq 5000$ were used for each curve. SG-3 wavelets were used throughout, and error calculations are done for 400 tracks of length 200 time points each, assuming diffusive stochastic motion ($\alpha = 1$). Analogous calculations for the fitted localization error ($\epsilon_{\rm fit}$) are shown in Fig. S6. To see this figure in color, go online.

larger wavelet spans (n), so that the drift velocity deviates significantly over the span of the wavelet. Restricting to shorter spans, however, limits the range of rescaled times, $\widehat{t}_k$, used in the analysis and thus leads to increased sampling error in the fitted parameters. The balance between these effects results in an optimal value of maximum span, $n_{\rm max}$, to be used for the fits (Fig. 2, *a* and *b*). We note that the optimal span depends on the shape of the wavelet, with wavelets that perform more aggressive smoothing yielding a higher value of $n_{\rm max}$. We select the wavelet shape (SG-3, the third-order Savitzky-Golay filter) used for all subsequent analyses based on minimizing the overall error in the fitted scaling parameter, $\alpha_{\rm fit}$ (Section S6). In the case where the drift velocity decorrelates much more slowly than the frame rate, a wide range of $n_{\rm max}$ will give consistent results for the estimated parameters characterizing the high-frequency stochastic motion.

The bias and error in the fit parameters depend on the relative magnitude of the stochastic motion and the drift velocity (Fig. 2, *c* and *d*), as well as the persistence time of the drift. When the persistence time is long ($\widetilde{\tau} > 10$), the MSD due to drift over one time step can be expanded into a term associated with constant drift ($\widetilde{\gamma}^2$) and a first-order correction ($\widetilde{\gamma}^2/\widetilde{\tau}$). The former term is effectively removed by the BNEW procedure. The relative bias in the fit parameters is then dependent on the displacement due to diffusion relative to the remaining displacement from drift. That is, the bias is determined by the compound parameter $\widetilde{\tau}\widetilde{D}/\widetilde{\gamma}^2$ (Fig. 2, *e* and *f*). To decrease bias below 10% for all fitted parameters, it is sufficient to have $\widetilde{D}\widetilde{\tau}/\widetilde{\gamma}^2 > 40$. When the bias is small, the overall error in the fit parameters is dominated by sampling error that depends entirely on the magnitude of diffusion relative to the localization error ($\widetilde{D}$), as well as the number of tracks sampled.

We further compare the performance of the BNEW method with the traditional approach of fitting the short-time portion of the total MSD curve, where the ballistic contribution from the drift velocity is least pronounced. For a wide range of parameters, BNEW outperforms the standard approach, yielding significantly less bias and error in the fitted parameters (Fig. 3). These calculations validate the ability of our methodology to accurately characterize stochastic motion in situations where there is sufficient drift velocity to dominate the overall MSD.

In the case where the stochastic component of the trajectories corresponds to fractional Brownian motion ($\alpha < 1$),

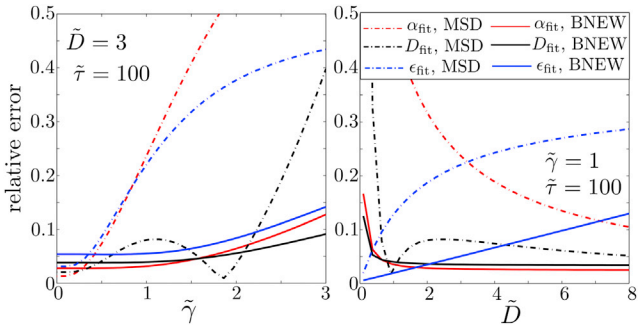

FIGURE 3 Comparison of error in fit parameters for high-frequency stochastic motion, using the BNEW method (*solid lines*) and ordinary MSD curves (*dashed lines*), as a function of drift magnitude, $\tilde{\gamma}$, for a constant diffusion coefficient $\tilde{D} = 3$ (*left panel*) and as a function of diffusion coefficient, $\tilde{D}$, for a constant $\tilde{\gamma} = 1$ (*right panel*). Drift is assumed to have a dimensionless correlation time of $\tilde{\tau} = 100$. Errors shown are for 400 tracks of length 200 time steps. BNEW analysis was done using SG-3 wavelets with spans of $2 \le n \le 17$. Errors for plain MSD curves were obtained from fits to $1 \le k \le 3$, the smallest number of points for fitting a power law. This fitting range minimizes error in the presence of drift (see Section S7). To see this figure in color, go online.

time-varying drift leads to a larger bias in the parameter estimation, and the BNEW method is applicable for a more limited range of parameters (Section S8). Nonetheless, it remains a substantially more accurate means of characterizing the stochastic motion than the traditional alternative of fitting ordinary MSD curves (Fig. S11).

A MATLAB software implementation of the BNEW method is provided in the Supporting Material.

Application to organelle movement in motile cells

As a biologically relevant example, we apply the BNEW method to analyze the trajectories of lysosomes in motile neutrophil-like HL60 cells. These organelles form a convenient endogenous probe of intracellular mechanics because they are punctate, numerous, and well dispersed throughout the cell. By analyzing the high-frequency component of the lysosome motion, we demonstrate that the cytoplasm of these cells behaves primarily as a viscous fluid over the timescales examined, with organelles undergoing apparent diffusion in the cytoplasm.

HL60 cells were placed in a 2D environment, confined under an agarose pad (27), in a uniform concentration of chemoattractant (see Materials and Methods). Under such conditions, these cells exhibit undirected but relatively persistent motility, with concomitant fluctuations in cell shape as they crawl (Fig. 4 *b*). Lysosomes within the cells were fluorescently labeled (Fig. 4 *a*), and the migrating cells were imaged with a time step of $\Delta = 0.05$ s.

The motion of the lysosomes is dominated by the overall migration of the cell, as well as the intracellular flows and cell shape deformation (Fig.4, *b* and *c*). This effect complicates the microrheological analysis of such tracks, making it impractical to characterize the viscosity or viscoelasticity of the intracellular medium using the MSD alone, even after correcting for whole-cell rigid body motion (Fig. 4 *d*). The BNEW method, however, makes it possible to extract material properties based on the high-frequency stochastic component of the motion,while filtering out the slowly varying flow. Trajectories for all particles within each cell are pooled together to obtain sufficient statistics, due to the limited length of individual trajectories (mean length 118 time steps).

The rescaled, corrected mean squared displacement, $\widehat{\mathrm{MSD}}_k^{(n)}$, for particles in several representative cells is shown in Fig. 4 *e*. We use a maximal wavelet span of $n_{\max} = 17$ for the BNEW analysis, a value selected based on a characterization of the population average drift velocities for particles in all cells pooled together (Section S9). The linear scaling of the $\widehat{\mathrm{MSD}}_k^{(n)}$ is consistent with diffusive motion of particles in a purely viscous medium.

We repeated the BNEW analysis for a population of 93 HL60 cells. After applying BNEW analysis to each cell, we calculated the distribution of the estimated scaling parameter $(\alpha_{\rm fit})$, diffusion coefficient $(D_{\rm fit})$, and localization error $(\epsilon_{\rm fit})$ among the population of cells (Fig. 5). Because we do not know a priori whether the stochastic motion of the particles in individual cells is diffusive or subdiffusive, we limit the time separations used in the fits to $k_{\max} = 0.74$ to avoid bias in the fitted scaling coefficient, α, for the subdiffusive case (Section S3). This conservative approach results in more noisy estimates, which may be partially responsible for the broad distribution of results over the entire population of cells.

The diffusion coefficient for lysosomes averaged among all cells has a value of $<D_{\rm fit}> = 0.018\ \mu\mathrm{m}^2/\mathrm{s}$, with a population standard deviation of $0.014\ \mu\mathrm{m}^2/\mathrm{s}$. This value is consistent with previous microrheological measurements of the diffusion coefficient within chemotaxing PMN cells (28). In general, lysosome size varies widely, with a typical diameter of about 0.5 μm (29). Using the Stokes-Einstein equation for the diffusion coefficient of a sphere (30), $(D = kT/(6\pi R\eta))$, gives an effective viscosity of $\eta \approx 50$ cP, or ~50 times that of water. We note, however, that this approximation assumes thermally driven particle motion, and that the actual viscosity may be significantly higher given a higher effective temperature due to actively generated forces (6,31).

The population averaged localization error was calculated as $<\epsilon_{\rm fit}> = 0.015\ \mu$m, consistent with control measurements in a fixed cell (Section S10). We note that the fitted parameters from running BNEW analysis on the full set of tracks from all cells pooled together (Fig. 5 *a*) are close to the average of individual cell measurements, confirming the robustness of the analysis.

The scaling exponent of the high-frequency component of motion extracted with the BNEW method is peaked around $\alpha_{\rm fit} = 1.02$, indicating that the average motion of lysosomes in the cytoplasm of most HL60 cells is consistent with diffusion in a purely viscous medium. However, the breadth of

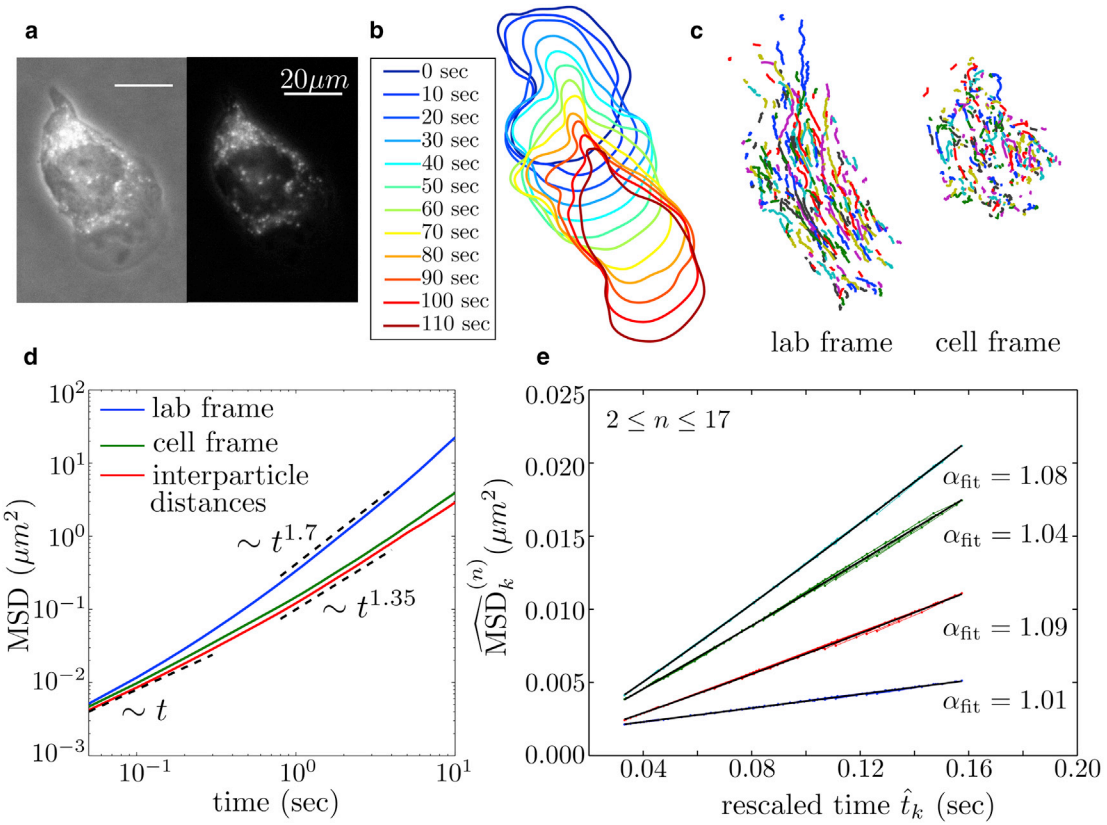

FIGURE 4 Analysis of lysosome trajectories in an HL60 cell. (*a*) Example cell with lysotracker labeling, imaged in consecutive frames with phase contrast in addition to fluorescence (*left*) and with fluorescence only (*right*). (*b*) Migrating cell shape over time. (*c*) Example lysosome trajectories in the lab frame of reference and in the cell frame of reference. (*d*) Mean-squared displacement for all tracked lysosomes in the example cell, in the lab frame (*blue*) and the cell frame (*green*). The mean-squared change in interparticle distances is shown in red. Dashed lines indicate scaling as a guide to the eye. (*e*) Rescaled, adjusted MSD after BNEW analysis for the example cell (*red*), and for other representative cells (*blue*, *green*, and *cyan*). Wavelet smoothing was done with SG-3 wavelets for spans of $2 \leq n \leq 17$. Black lines indicate power-law fits to Eq. 12 with the given scaling coefficients, α_{fit}. To see this figure in color, go online.

the distribution for α_{fit}, as well as D_{fit}, is far wider than would be expected based on simulated trajectory results, implying that the biological variability of individual cells is responsible for the broad range of values. Of particular interest are those cells with low values of α_{fit}, implying a potentially distinct cytoplasmic environment that leads to subdiffusive motion. Identifying the biophysical root of the difference in particle behavior within such cells, as compared to the majority of HL60 cells, is a promising avenue for further research. In this case, the BNEW method serves as a metric for identifying unusual cell subpopulations meriting further study.

DISCUSSION

The BNEW method enables the characterization of high-frequency motion from single-particle trajectories that are confounded by the presence of flow in the underlying medium. Because approximations of the flow velocity are subtracted out from individual tracks, no assumptions are imposed on the spatial structure of the flow. This method yields accurate approximations of the viscoelastic scaling modulus and the diffusion coefficient, provided the flow velocity varies slowly compared to the frame rate (see Fig. 2, *e* and *f*, for accuracy criteria).

Characterizing the stochastic component requires focusing on the short-time, high-frequency regime. For single-particle tracking experiments, the minimal timescale of observation is limited in practice to the millisecond regime, both by the camera frame rate and the spatial resolution in locating particles. Although other techniques, such as fluorescence correlation spectroscopy (32) and dynamic light scattering (33), are available for probing shorter timescales, they require significantly more complex experimental setup and are necessarily restricted to averages over the behavior of many particles. The BNEW method, on the other hand, requires only video microscopy of labeled particles, and is applicable to the analysis of individual long particle trajectories, provided sufficient data can be obtained through time averaging.

Prior studies aimed at analyzing short- versus long-timescale behavior in the trajectories of whole moving cells have made use of the Fourier-transformed velocity autocorrelation function to isolate different components of the

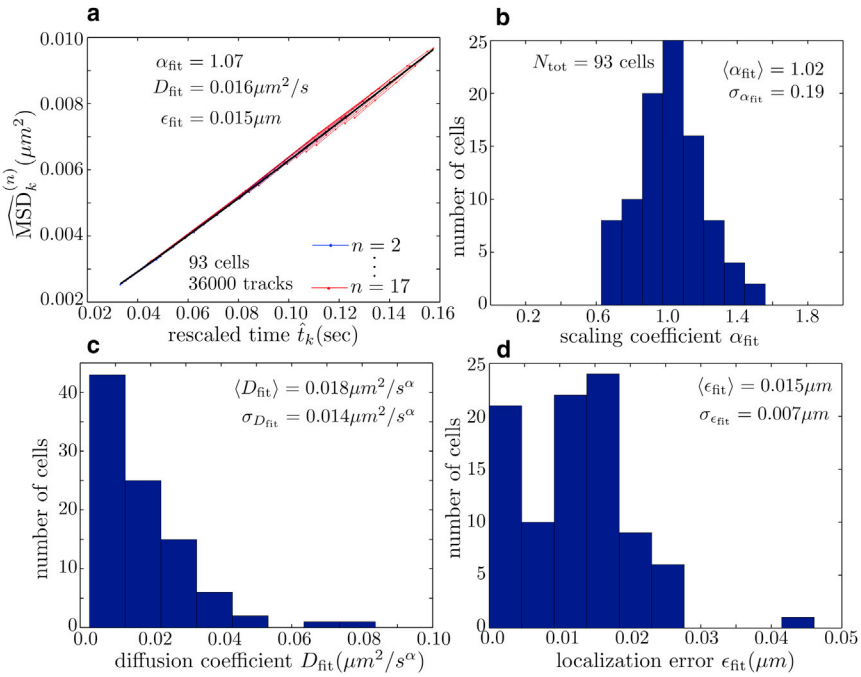

FIGURE 5 Statistics from BNEW analysis of lysosome motion in a population of 93 HL60 cells, with an average of 391 tracks each and an average track length of 118 time steps. SG-3 wavelets with spans of $2 \le n \le 17$ and time separations of $1 \le k \le \lfloor 0.74n \rfloor$ were used for the BNEW analysis. (*a*) Rescaled MSD from BNEW analysis of all tracks pooled together. The black line shows a power-law fit with the given parameters. (*b*) Histogram of scaling coefficients ($\alpha_{\rm fit}$) for pooled lysosome tracks from each individual cell. The population average ($\langle\alpha_{\rm fit}\rangle$) and standard deviation ($\sigma_{\alpha_{\rm fit}}$) are as shown. (*c*) Histogram of diffusion coefficients ($D_{\rm fit}$) from individual cells. (*d*) Histogram of fitted localization errors ($\epsilon_{\rm fit}$) from individual cells. Cases with $\epsilon_{\rm fit} = 0$ were excluded from the ensemble average and standard deviation calculations for the localization error. To see this figure in color, go online.

motion (34). In principle, this technique could be extended to particles moving through a viscoelastic medium by taking the discrete Fourier transform of the known velocity correlation function for such motion (35). The BNEW method, however, provides a related but more general approach, using wavelet analysis instead of Fourier transforms to perform the high-pass filtering of particle trajectories. In fact, the Fourier transform of a signal can be formulated as a particular wavelet shape with span equal to the full length of the signal. Wavelet analysis, however, is more naturally amenable to studying behaviors that are localized in time, and is thus the preferred choice for analyzing complex nonstationary signals (36). Furthermore, the limited span of the wavelets used makes it possible to combine data from trajectories of different lengths and to perform the analytic error analysis shown in Fig. 2.

The BNEW method enables characterization of material properties in nonquiescent media. Potential applications include not only the cytoplasm of moving cells, but also mucus and other biofluids in the presence of flow. The BNEW technique can also be used to correct for stage drift and flow effects in situations where only a small number of particles are visualized simultaneously, limiting the efficiency of standard dedrifting methods (22). In principle, the method described here can be extended to correct for persistent flow in other metrics used to analyze particle trajectories, such as the velocity autocorrelation function. Extension to two-particle or multiparticle correlative tracking data is also possible, although this would require additional assumptions about the spatial structure of the underlying flow.

SUPPORTING MATERIAL

Supporting Materials and Methods, Software, and fourteen figures are available at http://www.biophysj.org/biophysj/supplemental/S0006-3495(15)01165-0.

AUTHOR CONTRIBUTIONS

E.F.K. designed research, analyzed data, developed computational tools, and wrote the article. C.K.C designed and performed experiments. J.A.T. designed research and wrote the article.

ACKNOWLEDGMENTS

We thank Rikki M. Garner, Ahmad N. Nabhan, and Miranda Stratton for assistance with pilot experiments; and Stephanie C. Weber and Andrew J. Spakowitz for helpful comments on the manuscript.

E.F.K. was supported by the James S. McDonnell Foundation Postdoctoral Fellowship Award in Complex Systems; C.K.C. was supported by the Stanford Cellular and Molecular Biology Training grant (T32-GM007276); J.A.T. was funded by the Howard Hughes Medical Institute and the Stanford Center for Systems Biology (P50-GM107615).

SUPPORTING CITATIONS

References (37–44) appear in the Supporting Material.

REFERENCES

1. Schuster, B. S., J. S. Suk, …, J. Hanes. 2013. Nanoparticle diffusion in respiratory mucus from humans without lung disease. *Biomaterials.* 34:3439–3446.
2. Mizuno, D., C. Tardin, …, F. C. Mackintosh. 2007. Nonequilibrium mechanics of active cytoskeletal networks. *Science.* 315: 370–373.

3. Wirtz, D. 2009. Particle-tracking microrheology of living cells: principles and applications. *Annu. Rev. Biophys.* 38:301–326.
4. Weber, S. C., A. J. Spakowitz, and J. A. Theriot. 2010. Bacterial chromosomal loci move subdiffusively through a viscoelastic cytoplasm. *Phys. Rev. Lett.* 104:238102.
5. Kole, T. P., Y. Tseng, …, D. Wirtz. 2005. Intracellular mechanics of migrating fibroblasts. *Mol. Biol. Cell.* 16:328–338.
6. Weber, S. C., A. J. Spakowitz, and J. A. Theriot. 2012. Nonthermal ATP-dependent fluctuations contribute to the in vivo motion of chromosomal loci. *Proc. Natl. Acad. Sci. USA.* 109:7338–7343.
7. Parry, B. R., I. V. Surovtsev, …, C. Jacobs-Wagner. 2014. The bacterial cytoplasm has glass-like properties and is fluidized by metabolic activity. *Cell.* 156:183–194.
8. Daniels, B. R., B. C. Masi, and D. Wirtz. 2006. Probing single-cell micromechanics in vivo: the microrheology of *C. elegans* developing embryos. *Biophys. J.* 90:4712–4719.
9. Gal, N., and D. Weihs. 2012. Intracellular mechanics and activity of breast cancer cells correlate with metastatic potential. *Cell Biochem. Biophys.* 63:199–209.
10. Deng, W., and E. Barkai. 2009. Ergodic properties of fractional Brownian-Langevin motion. *Phys. Rev. E Stat. Nonlin. Soft Matter Phys.* 79:011112.
11. MacKintosh, F. C., and A. J. Levine. 2008. Nonequilibrium mechanics and dynamics of motor-activated gels. *Phys. Rev. Lett.* 100:018104.
12. MacKintosh, F. C. 2012. Active diffusion: the erratic dance of chromosomal loci. *P Natl Acad Sci.* 109:7138–7139.
13. Percival, D. B., and A. T. Walden. 2006. Wavelet Methods for Time Series Analysis, vol. 4. Cambridge University Press, Cambridge, United Kingdom.
14. Chevry, L., R. Colin, …, J.-F. Berret. 2013. Intracellular microrheology probed by micron-sized wires. *Biomaterials.* 34:6299–6305.
15. Yamada, S., D. Wirtz, and S. C. Kuo. 2000. Mechanics of living cells measured by laser tracking microrheology. *Biophys. J.* 78:1736–1747.
16. Valentine, M. T., Z. E. Perlman, …, D. A. Weitz. 2005. Mechanical properties of *Xenopus* egg cytoplasmic extracts. *Biophys. J.* 88: 680–689.
17. Wessel, A. D., M. Gumalla, …, C. F. Schmidt. 2015. The mechanical properties of early *Drosophila* embryos measured by high-speed video microrheology. *Biophys. J.* 108:1899–1907.
18. Seroussi, I., D. Veikherman, …, K. Keren. 2012. Segmentation and tracking of live cells in phase-contrast images using directional gradient vector flow for snakes. *J. Microsc.* 247:137–146.
19. Crocker, J. C., and D. G. Grier. 1996. Methods of digital video microscopy for colloidal studies. *J. Colloid Interface Sci.* 179:298–296.
20. Kilfoil, M. Matlab particle pretracking and tracking, and 2D feature finding. http://people.umass.edu/kilfoil/downloads.html.
21. Chen, K., B. Wang, …, S. Granick. 2013. Diagnosing heterogeneous dynamics in single-molecule/particle trajectories with multiscale wavelets. *ACS Nano.* 7:8634–8644.
22. Rowlands, C. J., and P. T. So. 2013. On the correction of errors in some multiple particle tracking experiments. *Appl. Phys. Lett.* 102:021913.
23. Schafer, R. W. 2011. What is a Savitzky-Golay filter? *IEEE Signal Process. Mag.* 28:111–117.
24. Weber, S. C., M. A. Thompson, …, J. A. Theriot. 2012. Analytical tools to distinguish the effects of localization error, confinement, and medium elasticity on the velocity autocorrelation function. *Biophys. J.* 102:2443–2450.
25. Tolić-Nørrelykke, I. M., E.-L. Munteanu, …, K. Berg-Sørensen. 2004. Anomalous diffusion in living yeast cells. *Phys. Rev. Lett.* 93:078102.
26. Guigas, G., C. Kalla, and M. Weiss. 2007. Probing the nanoscale viscoelasticity of intracellular fluids in living cells. *Biophys. J.* 93:316–323.
27. Renkawitz, J., K. Schumann, …, M. Sixt. 2009. Adaptive force transmission in amoeboid cell migration. *Nat. Cell Biol.* 11:1438–1443.
28. Felder, S., and Z. Kam. 1994. Human neutrophil motility: time-dependent three-dimensional shape and granule diffusion. *Cell Motil. Cytoskeleton.* 28:285–302.
29. Bandyopadhyay, D., A. Cyphersmith, …, C. K. Payne. 2014. Lysosome transport as a function of lysosome diameter. *PLoS One.* 9:e86847.
30. Berg, H. C. 1993. Random Walks in Biology. Princeton University Press, Princeton, NJ.
31. Guo, M., A. J. Ehrlicher, …, D. A. Weitz. 2014. Probing the stochastic, motor-driven properties of the cytoplasm using force spectrum microscopy. *Cell.* 158:822–832.
32. Weiss, M., H. Hashimoto, and T. Nilsson. 2003. Anomalous protein diffusion in living cells as seen by fluorescence correlation spectroscopy. *Biophys. J.* 84:4043–4052.
33. Pecora, R. 2000. Dynamic light scattering measurement of nanometer particles in liquids. *J. Nanopart. Res.* 2:123–131.
34. Li, L., E. C. Cox, and H. Flyvbjerg. 2011. "Dicty dynamics": Dictyostelium motility as persistent random motion. *Phys. Biol.* 8:046006.
35. Weber, S. C., J. A. Theriot, and A. J. Spakowitz. 2010. Subdiffusive motion of a polymer composed of subdiffusive monomers. *Phys. Rev. E Stat. Nonlin. Soft Matter Phys.* 82:011913.
36. Polikar, R. 1999. The story of wavelets. *IMACS/IEEE CSCC Proc., 3rd, Athens, Greece.* 3:5481–5486.
37. Savitzky, A., and M. J. Golay. 1964. Smoothing and differentiation of data by simplified least squares procedures. *Anal. Chem.* 36:1627–1639.
38. Kroese, D. P., and Z. I. Botev. 2013. Spatial process simulation. *In* Lectures on Stochastic Geometry, Spatial Statistics and Random Fields, Volume 2: Analysis, Modeling and Simulation of Complex Structures. V. Schmidt, editor. Springer International, Cham, Switzerland, pp. 369–404.
39. Turchin, P. 1998. Quantitative Analysis of Movement: Measuring and Modeling Population Redistribution in Animals and Plants. Sinauer, Sunderland, MA.
40. Selmeczi, D., S. Mosler, …, H. Flyvbjerg. 2005. Cell motility as persistent random motion: theories from experiments. *Biophys. J.* 89: 912–931.
41. Bouchiat, C., M. D. Wang, …, V. Croquette. 1999. Estimating the persistence length of a worm-like chain molecule from force-extension measurements. *Biophys. J.* 76:409–413.
42. Yamakawa, H. 2012. Helical Wormlike Chains in Polymer Solutions. Springer, New York.
43. Kariya, T., and H. Kurata. 2004. Generalized Least Squares. John Wiley & Sons, New York.
44. Michalet, X. 2010. Mean square displacement analysis of single-particle trajectories with localization error: Brownian motion in an isotropic medium. *Phys. Rev. E Stat. Nonlin. Soft Matter Phys.* 82:041914.

Supplementary Material

E. F. Koslover, C. K. Chan, and J. A. Theriot

S1. HAAR WAVELET

The Haar wavelet is commonly used to approximate velocities over different time-scales from noisy trajectories. For instance, it has been employed in single particle tracking studies to distinguish actively transported vesicles from those diffusing passively in the cytoplasm[1]. This wavelet is defined by the coefficients,

$$w_j = \frac{1}{n(n+1)} \begin{cases} 1 & \text{for } 0 < j \leq n \\ -1 & \text{for } -n \leq j < 0 \\ 0 & \text{for } j = 0. \end{cases} \tag{S1}$$

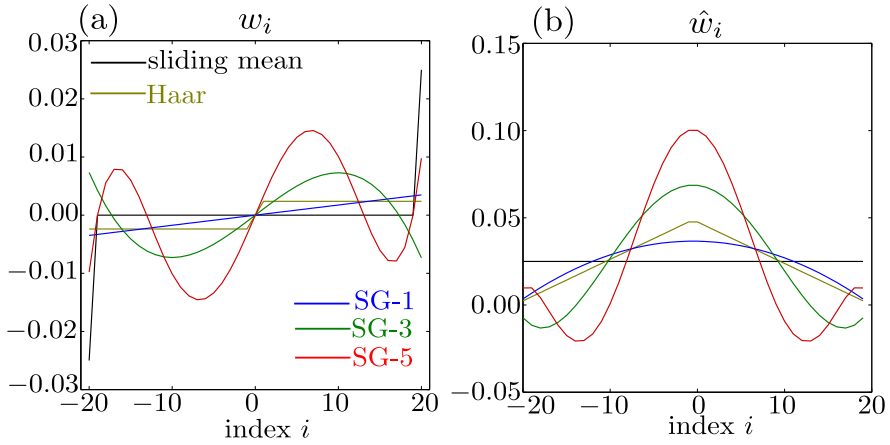

FIG. S1: Coefficients for different wavelet shapes, shown for span $n = 20$. (a) w_i coefficients for the trajectory positions. (b) $\hat{w}_i$ coefficients for the trajectory steps. Wavelet shapes shown are the sliding mean wavelet (black), Haar wavelet (yellow), and $1^{\text{st}}, 3^{\text{rd}}$, and 5^{th} order Savitzky-Golay wavelets (blue, green, and red, respectively).

The simple form of the Haar wavelet enables direct calculation of the summations in Eq. 10 to yield a closed form solution for the rescaling functions,

$$A^{(n)}_{k,\mathrm{Haar}} = \begin{cases} \frac{1}{60n^2(n+1)^2}\left[3k^5 - k^4(10n+5) + k^3(40n^2+40n-5) - k^2(80n^3+120n^2+30n-5)\right. & \\ \left. +k(60n^4+120n^3+80n^2+20n+2)\right] & \text{for } k \le n \\ \frac{1}{60n^2(n+1)^2}\left[-k^5 + k^4(10n+5) - k^3(40n^2+40n+5) + k^2(80n^3+120n^2+30n-5)\right. & \\ \left. -k(80n^4+160n^3+60n^2-20n-6) + (44n^5+110n^4+80n^3+10n^2-4n)\right] & \text{for } n < k < 2n \\ \frac{(2n+1)(3n^2+3n+4)}{30n(n+1)} & \text{for } k \ge 2n \end{cases} \tag{S2}$$

$$B^{(n)}_{k,\mathrm{Haar}} = \begin{cases} \frac{1}{n^2(n+1)^2}\left[-k^3 + k^2(2n+1) - 4kn(n+1) + 2n(n+1)(n^2+n+1)\right] & \text{for } k \le n \\ \frac{1}{3n^2(n+1)^2}\left[k^3 - 3k^2(2n+1) + 2k(6n^2+6n+1) + 2n^3(3n+4) - 12n^2(n+1) - 2n\right] & \text{for } n < k < 2n \\ \frac{6n^2-2n+2}{3n(n+1)} & \text{for } k \ge 2n \end{cases}$$

S2. SAVITZKY-GOLAY WAVELETS

The BNEW method relies on the drift velocity varying slowly in time, so that it can be effectively subtracted out by applying a wavelet that calculates a local estimate of the velocity across a window of span n. In the case where the drift velocity is not constant in time, one can estimate it more effectively by performing a less aggressive smoothing of the data. This can be done by either decreasing the span n, or by using a non-linear local approximation for the velocity. In either case, decreasing the smoothing also results in a more noisy estimate for the local velocity.

A common data smoothing technique uses the Savitzky-Golay filter[2], which involves fitting a local polynomial to each window of the data series. Higher-order polynomial fits provide less aggressive smoothing of the data. In practice, the Savitzky-Golay filter is applied by convolving each window of the data with a set of weights based on the least-square regression to the polynomial of a given degree[3]. Consequently, this smoothing technique can be formulated as a wavelet, with the particular set of weights w_i defined below.

To find the best-fit polynomial of degree d to data points p_i in a window $-n \le i \le n$, we can perform ordinary least-squares regression. The coefficients $a_0, \ldots, a_d$ of such a polynomial are given by

$$\vec{a} = (\mathbf{A}^T\mathbf{A})^{-1}\mathbf{A}^T\vec{p} \tag{S3}$$

where $\mathbf{A}$ is a $(2n+1) \times (d+1)$ matrix with $A_{i,j} = i^j, -n \le i \le n, 0 \le j \le d$. The local first derivative (velocity) approximation at the center of the window is given by a_1/Δ, where Δ is the time step. The weights for each of the data points used to compute this approximation are simply the second ($j = 1$) row of the matrix $(\mathbf{A}^T\mathbf{A})^{-1}\mathbf{A}^T$. That is, the Savitzky-Golay wavelet is defined by

$$\vec{w} = (0, 1, 0, \ldots, 0) \cdot (\mathbf{A}^T\mathbf{A})^{-1}\mathbf{A}^T. \tag{S4}$$

We note that since the best fit polynomial to a trajectory with constant velocity $p_i = yi + z$ has $a_1 = y$, then the required constraints on the wavelet shape (Eq. 4) are satisfied. It can be shown[3]

that the Savitzky-Golay filter for calculating first derivatives is identical for degree d and $d+1$ where d is an odd integer. We thus limit our discussion to filters of odd degree. The wavelet associated with the degree d Savitzky-Golay filter will be abbreviated as SG-d. The shape of such wavelets in terms of both the weights w_i associated with the positions and the equivalent weights $\hat{w}_i$ associated with the trajectory steps are plotted in Fig. S1. Unless otherwise noted, SG-3 wavelets are used throughout this work, for reasons discussed in Supplemental Section S6.

S3. BNEW ANALYSIS FOR FRACTIONAL BROWNIAN MOTION

We now analyze the behavior of the BNEW method when applied to particle trajectories where the stochastic component of the motion corresponds to fractional Brownian motion[4]. Discrete increments from a fractional Brownian motion process $\vec{p}(t)$ at time steps of size Δ are referred to as discrete fractional Brownian noise, and defined by

$$\vec{v}_i = \frac{\vec{p}[(i+1)\Delta] - \vec{p}[i\Delta]}{\Delta}. \tag{S5}$$

The $\vec{v}_i$ are identically normally distributed, with mean 0, variance $4D\Delta$, and covariance function (for $k \geq 1$) [5, 6]

$$\langle \vec{v}_i \cdot \vec{v}_{i+k} \rangle = 2D\Delta^{\alpha-2} \left(|k+1|^\alpha - 2|k|^\alpha + |k-1|^\alpha \right), \tag{S6}$$

This model is appropriate for thermal motion in a viscoelastic material. Note that throughout this work we assume that the stochastic motion occurs independently in each of two dimensions, though this approach can be easily extended to thre-dimensional trajectories. Sampling of discrete fractional Brownian noise for purposes of simulation was carried out using the circulant embedding approach for generating stationary processes[5].

When BNEW analysis is applied to a trajectory consisting of constant drift, fractional Brownian motion, and localization error, the adjusted MSD is derived from Eq. 6, 10 as

$$\begin{aligned} MSD_k^{(n)} = \left\langle |\vec{p}_k^{(n)} - \vec{p}_0^{(n)}|^2 \right\rangle =& 4D\Delta^\alpha A_k^{(n)} + 4\epsilon^2 B_k^{(n)} \\ &+ 4D\Delta^\alpha \sum_{i=-n}^{k+n-2} \sum_{j=1}^{k+n-2-i} c_i^{(n,k)} c_{i+j}^{(n,k)} \left((j+1)^\alpha - 2(j)^\alpha + (j-1)^\alpha \right), \end{aligned} \tag{S7}$$

where $c_i^{(n,k)}$ refers to the coefficients in Eq. 8 associated with a particular combination of wavelet span n and time separation k.

Rescaling the adjusted MSD by $B_k^{(n)}$ as for diffusive motion gives

$$\widehat{\mathrm{MSD}}_k^{(n)} = 4D\Delta^\alpha \tilde{A}_k^{(n)} + 4\epsilon^2, \tag{S8}$$

where $\tilde{A}_k^{(n)}$ is plotted as a function of the rescaled time $\hat{t}_k = A_k^{(n)}/B_k^{(n)}$ in Fig. S2a,b, for both the Haar wavelet and the 3$^{\mathrm{rd}}$ order Savitzky-Golay wavelet. The function $\tilde{A}_k^{(n)}$ depends on α and on the shape of the wavelet used, but not on the parameters D, ϵ.

We note that the results for different wavelet spans n collapse approximately onto a power-law curve, with downward "hooks" at larger values of k. So long as the maximal k values are relatively small compared to the span n, then $\tilde{A}_k^{(n)}$ can be approximately fit by the functional form,

$$\tilde{A}_k^{(n)} = f(\alpha)\hat{t}_k^\alpha + g(\alpha)^2 \tag{S9}$$

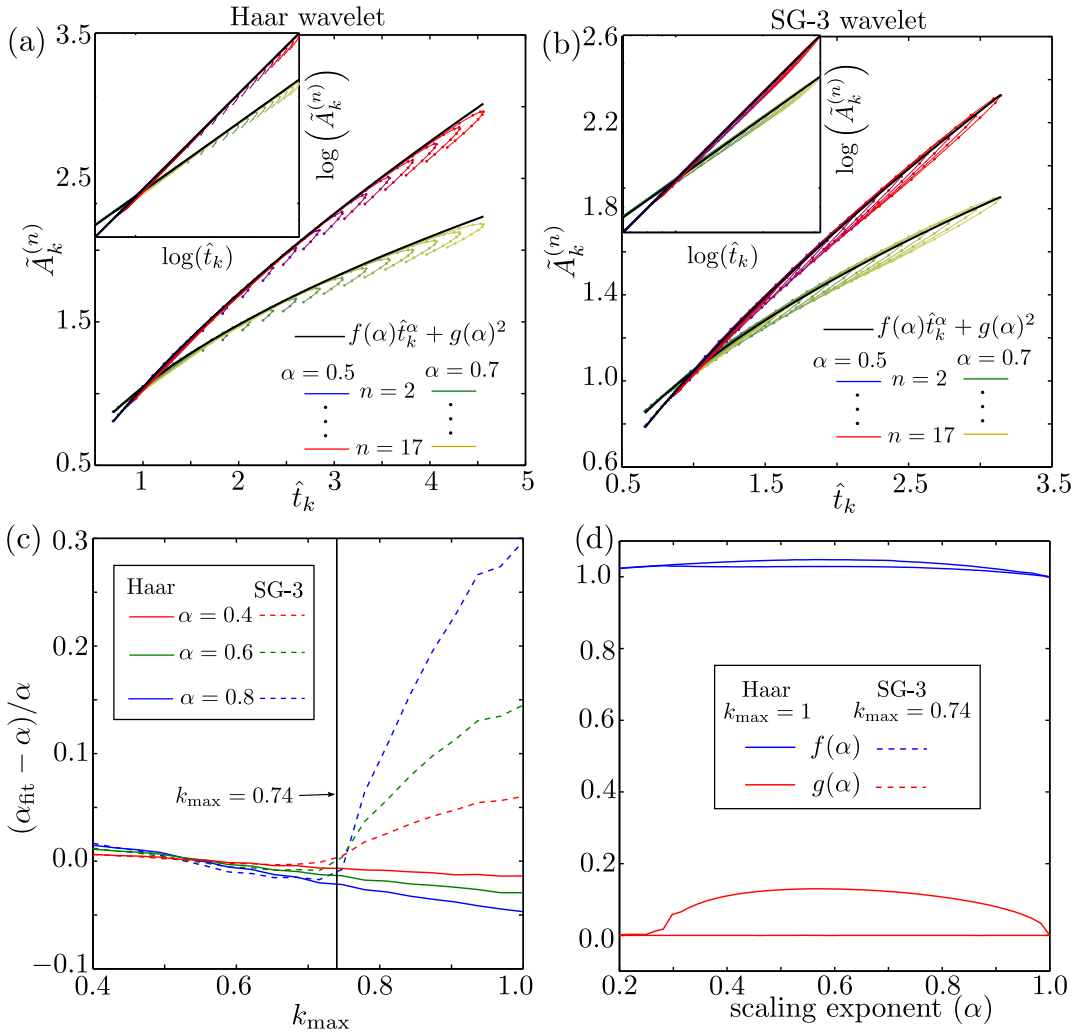

FIG. S2: BNEW analysis applied to trajectories consisting purely of fractional Brownian motion (no localization error or drift). (a) Function $\tilde{A}_k^{(n)}$ plotted against the rescaled time, for $\alpha = 0.5$ and $\alpha = 0.7$. Haar wavelet spans $2 \leq n \leq 17$ are included. Black lines correspond to the functional form in Eq. S9. Inset shows same data plotted on log-log axes. (b) Same results plotted using 3$^{\rm rd}$ order Savitzky-Golay (SG-3) wavelets for the wavelet analysis. (c) Fractional bias in fitted scaling exponent $\alpha_{\rm fit}$, as a function of maximal k value used in the fits, for Haar wavelets (solid lines) and SG-3 wavelets (dashed lines). (d) Function values $f(\alpha)$ (blue) and $g(\alpha)$ (red), for Haar wavelets (solid line) and SG-3 wavelets (dashed line), obtained by fitting $\tilde{A}_k^{(n)}$ to Eq. S9 for $2 \leq n \leq 17$, $1 \leq k \leq \lfloor k_{\rm max} n \rfloor$

.

We are interested primarily in extracting an accurate estimate of the viscoelastic scaling parameter α from such fits, in order to determine whether the particle motion is consistent with a viscous or a viscoelastic environment. Using wavelet spans $2 \leq n \leq 17$ for the fits, we plot the error in the parameter $\alpha_{\rm fit}$ depending on the maximal k values used in the fit. Specifically only values of k such that $1 \leq k \leq \lfloor k_{\rm max} n \rfloor$ are used for each span n. When fitting data from a limited number of trajectories, larger values of $k_{\rm max}$ would retain more information from the data, allowing for a less noisy fit. However, at higher values of $k_{\rm max}$, the downward "hooks" in the rescaled curves lead to incorrect estimations of the scaling parameter. We thus use the maximal value that allows for an accurate estimation of $\alpha_{\rm fit}$ (see Fig. S2c). Namely, $k_{\rm max} = 0.74$ is used for all data analysis using

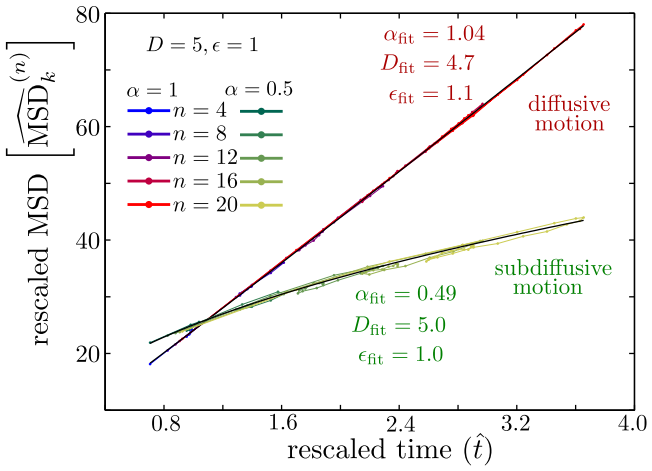

FIG. S3: Result of BNEW analysis with 3rd-order Savitzky-Golay wavelets on the same simulated trajectory dataset described in Fig. 1. Time separations $1 \leq k \leq \lfloor 0.74n \rfloor$ are shown for each wavelet span n. Fitted curves are shown in black, and the estimated values from the fits are listed for both the diffusive and the subdiffusive case.

3rd order Savitzky-Golay wavelets, while $k_{\rm max} = 1$ is used for analysis with Haar wavelets (*e.g.* Fig. 1).

The functions $f(\alpha)$ and $g(\alpha)$ are necessary for determining the effective diffusion coefficient (D) and localization error (ϵ), respectively. In particular the rescaled adjusted MSD is fit to,

$$\widehat{\rm MSD}_k^{(n)} = 4\hat{D}\Delta^\alpha \hat{t}_k^\alpha + 4\hat{\epsilon}^2, \tag{S10}$$

and the parameters D and ϵ are then extracted by

$$D_{\rm fit} = \frac{\hat{D}_{\rm fit}}{f(\alpha_{\rm fit})}, \tag{S11}$$

$$\epsilon_{\rm fit} = \sqrt{\hat{\epsilon}_{\rm fit}^2 - D_{\rm fit}\Delta^{\alpha_{\rm fit}} g(\alpha_{\rm fit})^2}. \tag{S12}$$

In the limit of diffusive motion ($\alpha = 1$), we have $f(1) = 1, g(1) = 0$, recovering Eq. 11. The functions f and g are determined numerically, by fitting $\tilde{A}_k^{(n)}$ as a function of $\hat{t}_k$ for $2 \leq n \leq 17$ for a range of α values (Fig. S2d).

The validity of this procedure for extracting estimates of α, D, ϵ to characterize the stochastic component of the motion is demonstrated for simulated trajectories in Fig. 1, using the Haar wavelet form. Analysis of the same trajectories with a 3rd order Savitzky-Golay wavelet is shown in Fig. S3.

S4. STATISTICS OF A PERSISTENT RANDOM WALK

To explore the effect of time-varying drift on the BNEW analysis method, we focus on a concrete model for the drift velocity as a continuous-time persistent random walk. This model has been used to describe the animal behavior[7], locomotion of motile cells[8], and paths of semiflexible polymers (where it is termed the worm-like chain)[9, 10]. It is appropriate for situations where there is a single characteristic timescale of persistence for the dynamical process. More complicated dynamics with multiple timescales can generally be expressed as sums of multiple persistent random walks.

One realization of a persistent random walk is motion with a constant speed (γ) along an orientation that varies diffusively in time with decorrelation time τ. In this section we derive some useful results regarding multi-point velocity correlations in this model. The propagator for the

persistent random walk in two dimensions satisfies

$$\frac{\partial G(\theta|\theta_0;t)}{\partial t} = \frac{1}{\tau}\frac{\partial^2 G(\theta|\theta_0;t)}{\partial \theta^2}, \tag{S13}$$

where $G(\theta|\theta_0;t)$ is the distribution of orientations for the velocity vector $\vec{u}$ at time t, given an orientation along θ_0 at time 0. This propagator can be expressed as

$$\begin{aligned} \partial G(\theta|\theta_0;t) &= \frac{1}{2\pi}\sum_{m=-\infty}^{\infty} g_m(t) e^{im(\theta-\theta_0)} \\ g_m(t) &= e^{-m^2 t/\tau}. \end{aligned} \tag{S14}$$

The velocity autocorrelation function is,

$$\begin{aligned} \langle \vec{u}(t)\vec{u}(0)\rangle =& \gamma^2 \int_0^{2\pi} d\theta \int_0^{2\pi} d\theta_0 \cos(\theta-\theta_0) G(\theta|\theta_0;t) \\ =& \frac{\gamma^2}{2}[g_1(t)+g_{-1}(t)] = \gamma^2 e^{-t/\tau} \end{aligned} \tag{S15}$$

At times shorter than the correlation time τ, the persistent random walk behaves like a ballistic motion with speed γ, while at longer times, the velocity orientation decorrelates and the motion appears diffusive with effective diffusion coefficient $\gamma^2\tau$. As a model for drift velocity, this formalism is convenient because it interpolates between constant drift ($\tau \to \infty$) and rapidly time varying drift $\tau \to 0$. In cases where the correlation time becomes comparable to the time step of the observed particle motion ($\tau \leq \Delta$), this drift velocity can no longer be distinguished from the diffusive component of the particle trajectories and BNEW analysis will not be accurate. In Fig. 2, we explore the bias and error introduced into the BNEW analysis in cases where the correlation time is finite but still much larger than the time step Δ.

In order to calculate errors in the fit parameters obtained with the BNEW method, we require also the fourth-order correlations in the particle velocities. For the persistent random walk, these correlations are given by,

$$\begin{aligned} \left\langle u_{i_0}^{(x)} u_{i_1}^{(x)} u_{i_2}^{(x)} u_{i_3}^{(x)} \right\rangle =& \left(\frac{\gamma}{2\pi}\right)^4 \int\int\int\int d\theta_0 d\theta_1 d\theta_2 d\theta_3 \cos\theta_0 \cos\theta_1 \cos\theta_2 \cos\theta_3 \\ & \times G(\theta_3|\theta_2,t_3) G(\theta_2|\theta_1,t_2) G(\theta_1|\theta_0,t_1) \\ =& \left(\frac{\gamma}{2}\right)^4 [2 g_1(t_1) g_2(t_2) g_1(t_3) + 4 g_1(t_1) g_0(t_2) g_1(t_3)] \\ =& \frac{\gamma^4}{4} e^{-(t_1+t_3)/\tau}\left[\frac{1}{2}e^{-4t_2/\tau}+1\right], \end{aligned} \tag{S16}$$

where $t_j = (i_j - i_{j-1})\Delta$ and the indices are ordered as $i_0 \leq i_1 \leq i_2 \leq i_3$. Similarly, we have

$$\begin{aligned} \left\langle u_{i_0}^{(x)} u_{i_1}^{(x)} u_{i_2}^{(y)} u_{i_3}^{(y)} \right\rangle &= \frac{\gamma^4}{4} e^{-(t_1+t_3)/\tau}\left[-\frac{1}{2}e^{-4t_2/\tau}+1\right] \\ \left\langle u_{i_0}^{(x)} u_{i_1}^{(y)} u_{i_2}^{(x)} u_{i_3}^{(y)} \right\rangle &= \left\langle u_{i_0}^{(x)} u_{i_1}^{(y)} u_{i_2}^{(y)} u_{i_3}^{(x)} \right\rangle = \frac{\gamma^4}{8} e^{-(t_1+4t_2+t_3)/\tau}, \end{aligned} \tag{S17}$$

and other combinations of the x, y dimensions can be obtained by symmetry.

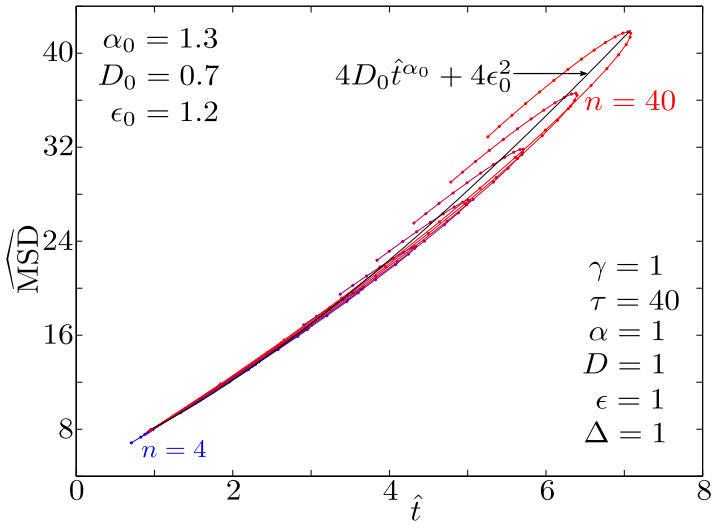

FIG. S4: Analytically calculated values of the rescaled adjusted MSD for trajectories consisting of persistent random walk drift with parameters $\tau = 40, \gamma = 1$, diffusive random motion ($\alpha = 1, D = 1$), and localization error ($\epsilon = 1$), sampled at time intervals of size $\Delta = 1$. SG-3 wavelets were used for the BNEW analysis, with spans between $n = 4$ and $n = 40$ (colored from blue to red). Black line corresponds to the power-law fit, showing the bias away from a linear function.

S5. ERROR ANALYSIS IN THE PRESENCE OF TIME-VARYING DRIFT

In this section, we calculate the bias and error in the fitted coefficients $\alpha_{\text{fit}}, D_{\text{fit}}, \epsilon_{\text{fit}}$, when the drift-velocity $\vec{u}$ varies in time as a persistent random walk (defined in Supplemental Section S4). Throughout this section, we restrict to the case with diffusive stochastic motion ($\alpha = 1$). The rescaled, adjusted MSD after BNEW analysis using wavelets of span n is

$$\widehat{\text{MSD}}_k^{(n)} = 4D\Delta t_k^{(n)} + 4\epsilon^2 + \frac{1}{B_k^{(n)}} \sum c_i^{(n,k)} c_j^{(n,k)} \langle \vec{u}_i \cdot \vec{u}_j \rangle \,, \tag{S18}$$

where $t_k^{(n)} = A_k^{(n)}/B_k^{(n)}$, as defined by Eq. 10, and the drift correlation function is given by Eq. S15, with $t = |i - j|\Delta$. The presence of the time-varying drift velocity causes the rescaled MSD curves for different wavelet spans to deviate from a universal line, increasing super-linearly and curling upwards at higher k values (Fig. S4). We find the bias in the fitted coefficients by fitting the power law Eq. 12 to the analytically calculated values of $\widehat{\text{MSD}}_k^{(n)}$ for $2 \le n \le n_{\max}$, $1 \le k \le \lfloor 0.74n \rfloor$. The parameter values from these fits are denoted $\alpha_0, \hat{D}_0, \hat{\epsilon}_0$.

In estimating the bias and the mean squared error of the fit parameters (described below), we linearize the fit function (Eq. 12) in terms of the parameters $\alpha, \hat{D}, \hat{\epsilon}$ in the neighborhood of $\alpha_0, \hat{D}_0, \hat{\epsilon}_0$. That is, we take

$$g(t_k^{(n)}, \vec{\chi}) \approx g(t_k^{(n)}, \vec{\chi}_0) + \mathbf{Z}(\vec{\chi} - \vec{\chi}_0), \quad Z_{i,j} = \frac{\partial g(t_i, \vec{\chi})}{\partial \chi_j}. \tag{S19}$$

Here, $\vec{\chi} = (\alpha, \hat{D}, \epsilon)$ is a vector of parameter estimates and $\mathbf{Z}$ is the matrix of partial derivatives of the fitted function g with respect to the parameters. This approximation is valid in the case where a large number of particle tracks are sampled, so that the measured MSD does not deviate far from the analytically calculated value (Eq. S18). In this case, the bias, defined as $\langle \vec{\chi}_{\text{fit}} - \vec{\chi} \rangle$ can be approximated as $\vec{\chi}_0 - \vec{\chi}$. The approximation breaks down in the case of limited sampling or when ϵ approaches 0, at which point additional bias inherent to the nonlinear regression can arise. To retain tractable error approximations, however, we focus on the linearizeable case. A comparison of bias and error estimates from simulated data as compared to our analytical approximations is shown in Fig. S5, for parameter values relevant to experimental data on lysosome motion in

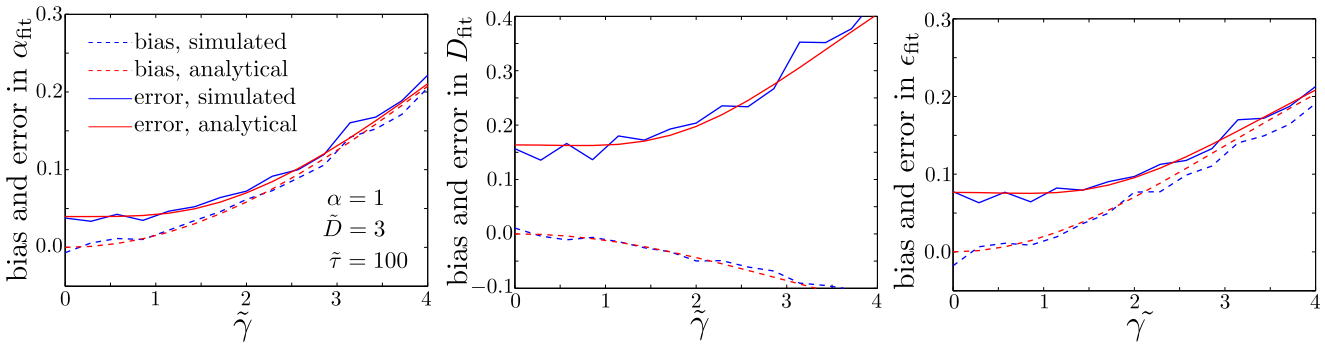

FIG. S5: Comparison of bias (dashed lines) and root mean squared error (solid lines) in fitted parameters $(\alpha_{\rm fit}, D_{\rm fit}, \epsilon_{\rm fit})$ as a function of dimensionless drift magnitude $\tilde{\gamma}$. Blue curves are from simulated data; red curves are from approximate analytical calculations. Errors are calculated for 200 trajectories of length 200 timepoints, with dimensionless parameters $\alpha = 1, \tilde{D} = 3, \tilde{\tau} = 100$, using SG-3 wavelets with spans $2 \leq n \leq 17$. Simulated values were averaged over 100 datasets.

.

HL60 cells (see Results section). We note that due to the presence of time-varying drift and the assumption of diffusive stochastic motion, we have $\alpha_0 \geq \alpha = 1$, so that we take $D_{\rm fit} = \hat{D}_{\rm fit}$, and $\epsilon_{\rm fit} = \hat{\epsilon}_{\rm fit}$ when calculating the bias and error.

We calculate an estimation of the total mean squared error (S^2) in the fitted parameters as,

$$S_\alpha^2 = (\alpha_0 - \alpha)^2 + \left\langle (\alpha_{\rm fit} - \alpha_0)^2 \right\rangle \tag{S20}$$

$$S_D^2 = (D_0 - D)^2 + \left\langle (D_{\rm fit} - D_0)^2 \right\rangle \tag{S21}$$

$$S_\epsilon^2 = (\epsilon_0 - \epsilon)^2 + \left\langle (\epsilon_{\rm fit} - \epsilon_0)^2 \right\rangle, \tag{S22}$$

where the first term arises from the bias due to deviation of the rescaled MSD from a universal line and the second term arises from noise in the sampled values. The brackets $\langle \ldots \rangle$ indicate averaging over a large set of trajectories, with fitted parameters extracted from the pooled set. These noise terms are taken from the diagonal of the covariance matrix of the fitted parameters, calculated as described below.

Under the linearization assumption, the covariance matrix of fitted parameters from performing a non-linear least-square fit to Eq. 12 is given by[11],

$$\mathbf{E} = (\mathbf{Z}'\mathbf{Z})^{-1}\mathbf{Z}'\mathbf{M}\mathbf{Z}(\mathbf{Z}'\mathbf{Z})^{-1}, \tag{S23}$$

where $\mathbf{M}$ is the covariance matrix of the individual data points used in the fit and $\mathbf{Z}$ is the matrix of partial derivatives of the fitted function with respect to the fit parameters. Namely,

$$\begin{aligned} Z_{m,\alpha} &= 4D_0(\Delta\hat{t}_m)^{\alpha_0} \log\left(\Delta\hat{t}_m\right), \\ Z_{m,\hat{D}} &= 4(\Delta\hat{t}_m)^{\alpha_0} \\ Z_{m,\hat{\epsilon}} &= 4\epsilon_0 \end{aligned} \tag{S24}$$

where the index m runs over all individual data points used for fitting, including all combinations of wavelet span n and time interval k for the rescaled adjusted MSD.

Calculating the covariance of the individual data points is complicated by the fact that each

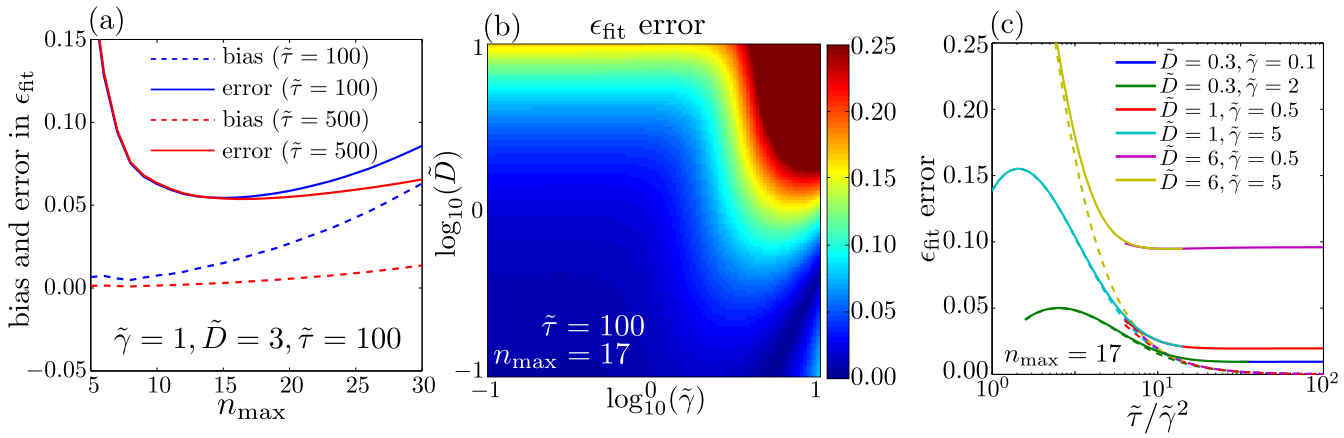

FIG. S6: Bias and root mean square error in the estimated value of the localization error $\epsilon_{\rm fit}$. (a) Bias (dashed curves) and error (solid curves) plotted as a function of maximal wavelet span $n_{\rm max}$, for $\tilde{D}=3, \tilde{\gamma}=1$, shown for drift correlation time $\tilde{\tau}=100$ (blue) and $\tilde{\tau}=500$ (red). (b) Root mean square error as a function of the dimensionless diffusion constant $\tilde{D}$ and drift magnitude, $\tilde{\gamma}$, assuming a persistece time of $\tilde{\tau}=100$. (c) Bias and error as a function of the compound parameter $\tilde{\tau}/\tilde{\gamma}^2$. SG-3 wavelets were used throughout and errors are calculated assuming 400 tracks of length 200 timesteps each.

adjusted MSD includes an average over many tracks and many time windows from each individual track. For simplicity, we assume in our error estimates that the individual particle tracks are completely independent from each other. Time averaging in the MSD calculation, however, can involve many non-independent intervals, and the co-dependence of these intervals must be taken into account when calculating data point covariance. We focus on the time average only, noting that the elements of the covariance matrix simply scale inversely with the number of tracks in the ensemble average, assuming individual tracks are independent of each other. For a track composed of $N+1$ sequential positions $\vec{p}_0, \ldots, \vec{p}_N$, the adjusted mean scaled displacement (for a span n and time separation k) is given by

$$\begin{aligned} \mathrm{MSD}_k^{(n)} &= \frac{1}{\mathcal{N}_k} \sum_{l=n_{\rm max}}^{N-n_{\rm max}-k} \eta_l^{(n,k)}, \\ \eta_l^{(n,k)} &= \left| \bar{p}_{l+k}^{(n)} - \bar{p}_l^{(n)} \right|^2 \\ &= \left| \Delta \sum_{i=-n}^{k+n-2} c_i^{(n,k)} \left(\vec{u}_{l+i} + \vec{v}_{l+i}\right) + \sum_{i=-n}^{k+n-1} \hat{c}_i^{(n,k)} \xi_{l+i} \right|^2 \\ \mathcal{N}_k &= N - k - 2n_{\rm max} + 1 \end{aligned} \tag{S25}$$

where the first and last $n_{\rm max}$ data points are dropped for all the different wavelet spans $n \le n_{\rm max}$ used in the BNEW analysis to avoid edge effects. The covariance matrix elements for the rescaled MSD are then,

$$\begin{aligned} M_{m_1,m_2} &= \frac{\mathrm{cov}\left(\mathrm{MSD}^{(m_1)}, \mathrm{MSD}^{(m_2)}\right)}{B^{(m_1)} B^{(m_2)}} \\ &= \frac{\sum_{l_1,l_2} \mathrm{cov}\left(\eta_{l_1}^{(m_1)}, \eta_{l_2}^{(m_2)}\right)}{B^{(m_1)} B^{(m_2)} \mathcal{N}_{k_1} \mathcal{N}_{k_2}} \end{aligned} \tag{S26}$$

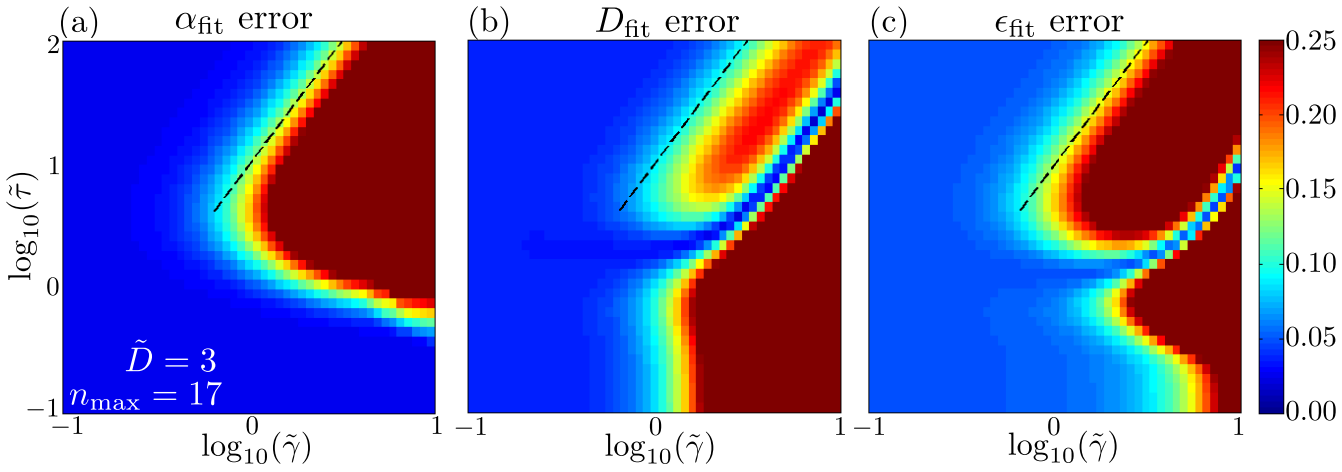

FIG. S7: Root mean square error in fit parameters (a) $\alpha_{\rm fit}$, (b) $D_{\rm fit}$, (c) $\epsilon_{\rm fit}$, as a functin of dimensionless magnitude ($\tilde{\gamma}$) and correlation time $\tilde{\tau}$ of the drift velocity. All calculations use SG-3 wavelets with spans $2 \leq n \leq 17$, assuming 400 tracks of length 200 timesteps each. Dashed black lines mark a constant value of $\tilde{\tau}/\tilde{\gamma}^2$.

where, again, the m indices refer to pairs of wavelet spans n and time separations k. Noting that the average $\langle \eta_{l_1} \eta_{l_2} \rangle$ depends only on the difference between the indices ($q = l_1 - l_2$), and assuming diffusive stochastic motion ($\langle \vec{v}_i \cdot \vec{v}_j \rangle = 0$ for $i \neq j$), it can be shown that

$$\begin{aligned}\mathrm{cov}\left(\eta_l^{(m_1)}, \eta_{l+q}^{(m_2)}\right) =& (\gamma\Delta)^4 H^{(u)}_{m_1,m_2}(q) + (2D\Delta)^2 H^{(v)}_{m_1,m_2}(q) + \epsilon^4 H^{(\xi)}_{m_1,m_2}(q) + 4\gamma^2 D\Delta^3 F^{(u)}_{m_1,m_2}(q) F^{(v)}_{m_1,m_2}(q) \\ &+ 2\gamma^2\epsilon^2\Delta^2 F^{(u)}_{m_1,m_2}(q) F^{(\xi)}_{m_1,m_2}(q) + 4D\epsilon^2\Delta F^{(v)}_{m_1,m_2}(q) F^{(\xi)}_{m_1,m_2}(q),\end{aligned} \tag{S27}$$

where the $\mathbf{H}$ and $\mathbf{F}$ matrices that couple drift velocity, diffusion, and localization error across time steps are defined below. The fourth-order covariance of the drift velocity is

$$H^{(u)}_{m_1,m_2}(q) = \frac{1}{\gamma^4} \sum_{i_1,j_1,i_2,j_2} c_{i_1}^{(m_1)} c_{j_1}^{(m_1)} c_{i_2}^{(m_2)} c_{j_2}^{(m_2)} \mathrm{cov}\left(\vec{u}_{i_1} \cdot \vec{u}_{j_1}, \vec{u}_{i_2+q} \cdot \vec{u}_{j_2+q}\right) \tag{S28}$$

whose matrix elements can be calculated using Eq. S15, S16, S17. The corresponding covariance matrices $\mathbf{H}^v$, $\mathbf{H}^\xi$ for the diffusive velocities and localization errors, respectively, can be simplified to

$$\begin{aligned} H^{(v)}_{m_1,m_2}(q) &= 4\sum_{i\in T}\left[c_i^{(m_1)} c_{i-q}^{(m_2)}\right]^2 + 8\sum_{i,j\in T; j>i} c_i^{(m_1)} c_j^{(m_1)} c_{i-q}^{(m_2)} c_{j-q}^{(m_2)} \\ H^{(\xi)}_{m_1,m_2}(q) &= 4\sum_{i\in T}\left[\hat{c}_i^{(m_1)} \hat{c}_{i-q}^{(m_2)}\right]^2 + 8\sum_{i,j\in T; j>i} \hat{c}_i^{(m_1)} \hat{c}_j^{(m_1)} \hat{c}_{i-q}^{(m_2)} \hat{c}_{j-q}^{(m_2)} \end{aligned}$$

where the range of indices in the summations is $T = [\max(-n_1, -n_2+q), \min(n_1+k_1-1, n_2+k_2-1+q)]$ and $c^{(n,k)}_{n+k-1} = 0$ by convention. In the above, we make use of the fact that both the diffusive velocities and the localization errors in each dimension are independent and normally distributed with mean 0, and that the fourth moment of a normal distribution is three times the variance.

Due to the independence between different components of the particle motion (drift, diffusion,

and localization error), the cross-covariance terms can be factored into individual second-order correlations. For instance,

$$\mathrm{cov}\left(\vec{u}_{i_1}\cdot\vec{v}_{j_1},\vec{u}_{i_2+q}\cdot\vec{v}_{j_2+q}\right)=\frac{1}{2}\left\langle\vec{u}_{i_1}\cdot\vec{u}_{i_2+q}\right\rangle\left\langle\vec{v}_{i_1}\cdot\vec{v}_{i_2+q}\right\rangle, \tag{S29}$$

where the factor of $1/2$ arises from the two independent dimensions of the diffusive velocity. We therefore define the following quantities to complete the covariance calculation in Eq. S27:

$$\begin{aligned}
F^{(u)}_{m_1,m_2}(q) &= \frac{1}{\gamma^2}\sum_{i_1,i_2} c_{i_1}^{(m_1)}c_{i_2}^{(m_2)}\left\langle\vec{u}_{i_1}\cdot\vec{u}_{i_2+q}\right\rangle \\
&= \sum_{i_1,i_2} c_{i_1}^{(m_1)}c_{i_2}^{(m_2)}e^{(-|i_2+q-i_1|\Delta/\tau)} &\text{(S30)}\\
F^{(v)}_{m_1,m_2}(q) &= 2\sum_{i\in T} c_i^{(m_1)}c_{i-q}^{(m_2)} &\text{(S31)}\\
F^{(\xi)}_{m_1,m_2}(q) &= 2\sum_{i\in T} \hat{c}_i^{(m_1)}\hat{c}_{i-q}^{(m_2)} &\text{(S32)}
\end{aligned}$$

The indices in Eq. S30 are taken from the range $-n_1\le i_1\le n_1+k_1-2, -n_2\le i_2\le n_2+k_2-2$. After computing the matrices $\mathbf{H}^{(u)},\mathbf{H}^{(v)},\mathbf{H}^{(\xi)},\mathbf{F}^{(u)},\mathbf{F}^{(v)},\mathbf{F}^{(\xi)}$, the covariance matrix $\mathbf{M}$ for the time-averaged, rescaled MSD can be calculated with the aid of Eq. S27 via

$$\begin{aligned}
M_{m_1,m_2} =& \frac{1}{B^{(m_1)}B^{(m_2)}\mathcal{N}_{k_1}\mathcal{N}_{k_2}}\Big[\min\left(\mathcal{N}_{k_1},\mathcal{N}_{k_2}\right)\mathrm{cov}\left(\eta_l^{(m_1)},\eta_l^{(m_2)}\right)+ \\
&+\sum_{q=1}^{\mathcal{N}_{k_2}-1}\min\left(\mathcal{N}_{k_1},\mathcal{N}_{k_2}-q\right)\mathrm{cov}\left(\eta_l^{(m_1)},\eta_{l+q}^{(m_2)}\right)+\sum_{q=1}^{\mathcal{N}_{k_1}-1}\min\left(\mathcal{N}_{k_2},\mathcal{N}_{k_1}-q\right)\mathrm{cov}\left(\eta_l^{(m_2)},\eta_{l+q}^{(m_1)}\right)\Big]
\end{aligned} \tag{S33}$$

We note that while the individual $\mathbf{H}^{(u)}(q)$ matrices are time-consuming to compute for any given value of the drift velocity correlation time τ, this computation need be done only once to find the covariance as a function of the remaining parameters (γ, D, ϵ).

The bias and error in the fitted scaling exponent α_{fit} and diffusion coefficient D_{fit} are shown in Fig. 2. The corresponding results for the fitted localization error ϵ_{fit} are plotted in Fig. S6. We note that the bias in the estimated localization error is determined primarily by the mean square displacement due to the time-varying component of the drift velocity that does not get corrected by the BNEW analysis. Thus, for cases with long correlation time ($\tilde{\tau}>10$) and relatively small drift, this bias is a function of the compound parameter $\tilde{\tau}/\tilde{\gamma}^2$ (Fig. S6c). When the effect of drift velocity is small, the overall error in ϵ_{fit} is determined by the sampling error, which increases with increasing $\tilde{D}$ (increasing magnitude of diffusion relative to localization error).

For less persistent drift ($1<\tau<10$), the bias in the scaling exponent drops back down as the persistent random walk itself approaches diffusive behavior over the timespan of the wavelet (Fig. S7a). As the persistence time becomes small relative to the time step ($\tau\lesssim 1$) the drift velocity as treated here (with displacement over each discrete step given by $\Delta\vec{u}_i$) approaches a chain of freely jointed steps. The average fitted diffusion coefficient then approaches the sum of the true diffusion and the effective diffusion arising from the drift ($\tilde{D}_0\approx\tilde{D}+\tilde{\gamma}^2/4$). The relative bias in D_{fit} goes to $\gamma^2/4D$ for small $\tilde{\tau}$ (Fig. S7b).

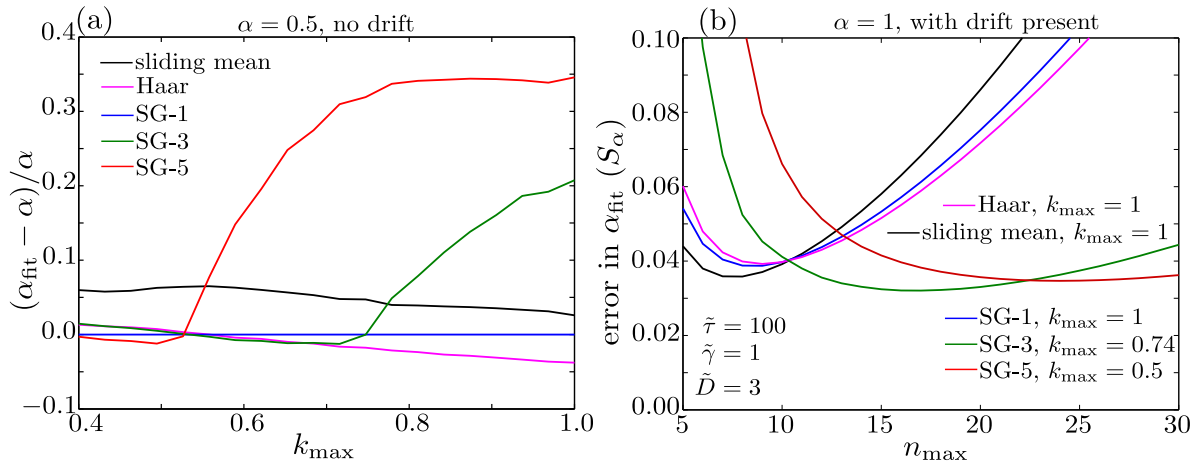

FIG. S8: Selecting optimal wavelet shape based on error estimates. (a) Fractional error in fitted exponent for the case of pure fractional Brownian motion, for different wavelet shapes, analogous to Fig. S2c. Fits are done for wavelet spans $2 \leq n \leq 17$ and $1 \leq k \leq \lfloor k_{\rm max} n \rfloor$. (b) Overall root mean squared error in the fitted scaling parameter for different wavelet shapes, as a function of maximal allowed wavelet span $n_{\rm max}$. The range of time separations k used for the fitting is selected based on panel (a). Errors are calculated assuming 400 trajectories of length 200 steps each.

S6. SELECTION OF WAVELET SHAPE

To select among a number of possible wavelet forms for use in BNEW analysis, we compare the estimated total error in the viscoelastic scaling $\alpha_{\rm fit}$ for a specific set of parameters relevant to the experimental data discussed in the Results section. The wavelet forms considered (plotted in Fig.S1) include the simplest sliding mean wavelet (characterized by constant step weights $\hat{w}_i = 1/(2n)$), the Haar wavelet (Supplemental Section S1), and different order Savitzky-Golay wavelets (SG-1, SG-3, SG-5, defined in Supplemental Section S2). The error in the fitted parameters depends additionally on the choice of $k_{\rm max}$, which sets how many time separations are considered for each wavelet span ($1 \leq k \leq \lfloor k_{\rm max} n \rfloor$). While increasing $k_{\rm max}$ up to $k_{\rm max} = 1$ will generally decrease the total error, it can also lead to over-estimating the scaling coefficient α in the case of subdiffusive stochastic motion, as discussed in Section S3. When fitting experimental data, we do not know *a priori* whether the particles are moving in a viscous or a viscoelastic medium, and thus want to avoid this source of bias in the α estimates. Consequently, while we use $k_{\rm max} = 1$ for the sliding mean, Haar, and SG-1 wavelets, we set $k_{\rm max} = 0.74$ for the SG-3 wavelet, and $k_{\rm max} = 0.5$ for the SG-5 wavelet, so that in the absence of drift, the scaling can be accurately characterized by $\alpha_{\rm fit}$ (see Fig.S8a and S2c). As plotted in Fig. S8b, the SG-3 wavelet gives the lowest error in the scaling estimate at an appropriately selected $n_{\rm max}$. These 3$^{\rm rd}$-order Savitzky-Golay wavelets are used throughout this work, unless otherwise specified. We note that increasing the degree of the polynomial fit in the SG wavelets also increases the optimal $n_{\rm max}$ as the less aggressive data smoothing more effectively subtracts out a time-varying drift. Selection of the appropriate $n_{\rm max}$ is discussed in Section S9.

S7. ERRORS FROM FITTING ORDINARY MSD CURVES

In order to compare the performance of the BNEW method to the traditional approach of fitting uncorrected mean squared displacement curves, we calculate the error in the fit parameters for the

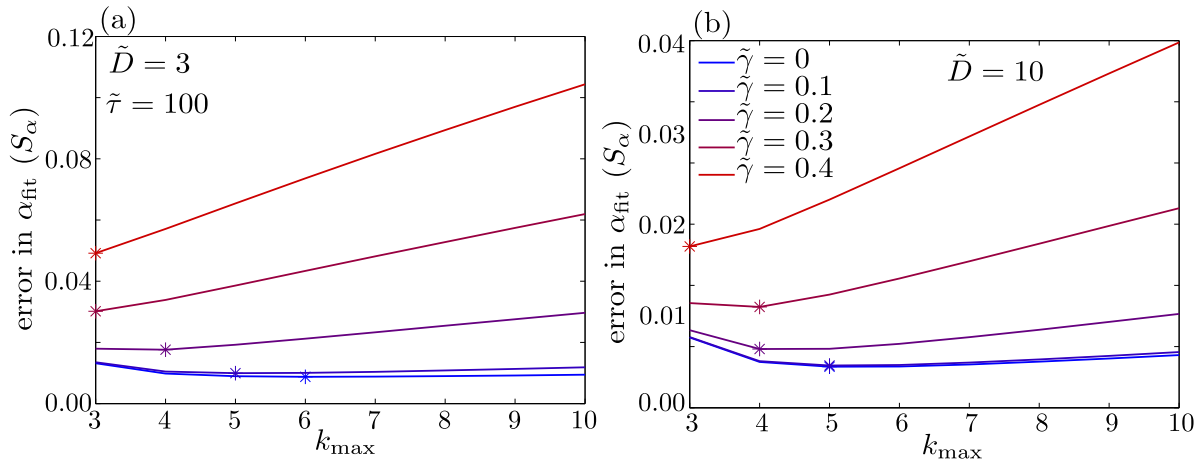

FIG. S9: Root mean squared error (S_α) in the fitted scaling parameter using ordinary MSD curves, without BNEW analysis. Time points $1 \leq k \leq k_{\rm max}$ are used for fitting. (a) For dimensionless diffusion constant $\tilde{D} = 3$, plotted for several values of drift velocity magnitude $\tilde{\gamma}$. Starred points indicate optimal value of $k_{\rm max}$ for each drift velocity. (b) For diffusion constant $\tilde{D} = 10$ with the same values of drift velocity. Errors are calculated assuming 400 trajectories with 200 timepoints each.

latter approach in the presence of drift velocities that behave as a persistent random walk. These errors can be obtained by applying the analysis in Section S5 with the "null" wavelet defined by $w_i = 0$. The corresponding scaling functions are $A_k = k, B_k = 1$, so that in the absence of drift, the rescaled MSD takes the form of the traditional mean-squared displacement,

$$\widehat{\rm MSD}_k = 4Dk + 4\epsilon^2. \tag{S34}$$

The drift velocity results in biased estimation of the parameters for stochastic motion, and the bias becomes more pronounced if a larger range of time separations k is used for the fit. For non-trivial magnitudes of the drift, the smallest mean squared error in the estimated parameters is achieved by taking the lowest possible $k_{\rm max} = 3$ (Fig. S9). This is the value used for the comparison to BNEW analysis in Fig. 3. It is interesting to note that even in the absence of persistent drift ($\gamma = 0$), the optimal range of k when fitting ordinary MSD curves is quite small: $k_{\rm max} = 6$ for tracks of length 200 timepoints, with $\tilde{D} = 3$, and even smaller values for higher dimensionless diffusion constant $\tilde{D}$. This effect has been pointed out previously based on similar calculations of the error associated with performing regressions on mean squared displacement curves.[12]

S8. BNEW ANALYSIS OF FRACTIONAL BROWNIAN MOTION WITH TIME-VARYING DRIFT

In the case where the stochastic component of the particle trajectories corresponds to fractional Brownian motion, the BNEW method is more sensitive to time varying drift than in the purely diffusive case. Intuitively, this is to be expected, since fractional Brownian motion results in smaller overall displacement of the particle relative to the drift, thus making this component of the motion more difficult to isolate for a given set of parameters $\tilde{\gamma}, \tilde{\tau}, \tilde{D}$. The bias in the estimated parameter values can be calculated by fitting the power-law curve to the analytical equation for rescaled

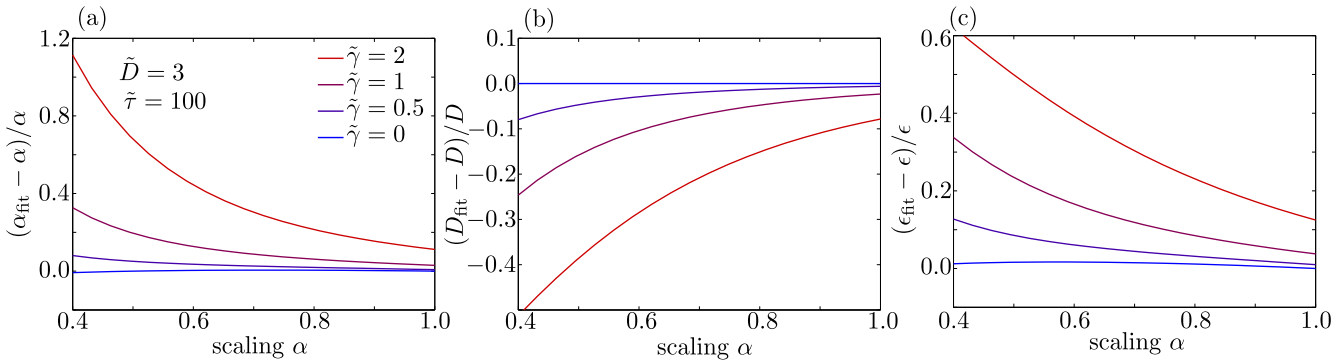

FIG. S10: Relative bias in fitted parameters from BNEW analysis of trajectories composed of fractional Brownian motion, localization error, and persistent random drift (with correlation time $\tilde{\tau} = 100$ and magnitude $\tilde{\gamma}$). (a) Bias in scaling exponent α; (b) bias in diffusion coefficient D; (c) bias in localization error ϵ. Dimensionless units are used throughout. SG-3 wavelets with spans $2 \leq n \leq 17$ and time separations $1 \leq k \leq \lfloor 0.74n \rfloor$ are used for the fits.

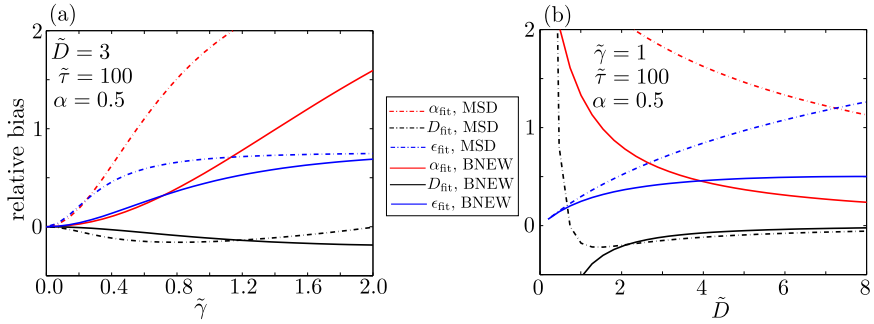

FIG. S11: Relative bias in fitted parameters from BNEW analysis (solid lines) as compared to fitting ordinary MSD curves (dashed lines), for trajectories composed of fractional Brownian motion (with scaling $\alpha = 0.5$), localization error, and persistent random drift (with correlation time $\tilde{\tau} = 100$ and magnitude $\tilde{\gamma}$). (a) Plotted versus drift magnitude; (b) plotted versus diffusion coefficient. Dimensionless units are used throughout. SG-3 wavelets with spans $2 \leq n \leq 17$ and time separations $1 \leq k \leq \lfloor 0.74n \rfloor$ are used for the fits.

MSD,

$$\widehat{\mathrm{MSD}}_k^{(n)} = 4D\Delta\tilde{A}_k^{(n)} + 4\epsilon^2 + \frac{1}{B_k^{(n)}} \sum c_i^{(n,k)} c_j^{(n,k)} \left\langle \vec{u}_i \cdot \vec{u}_j \right\rangle , \tag{S35}$$

where $\tilde{A}$ is defined by Eq. S7, S8. The power-law fits are done as a function of $t_k^{(n)}$.

The bias in the fitted coefficients is plotted as a function of the scaling exponent α for the fractional Brownian motion in Fig. S10. We note that for smaller values of α, the magnitude of drift velocity ($\tilde{\gamma}$) at which the BNEW analysis can give accurate estimates is more limited. Nonetheless, the accuracy of this method remains significantly better than fitting ordinary MSD curves for small magnitude drift (Fig. S11). We note that the advantage of the BNEW method in this case is particularly striking when determining the scaling coefficient $\alpha_{\rm fit}$, which can be estimated to within 50% for $\tilde{\gamma} < 1$ (when $\tilde{D} = 3, \tilde{\tau} = 100$). A fit of the ordinary MSD curve would require $\tilde{\gamma} < 0.3$ for the same level of accuracy.

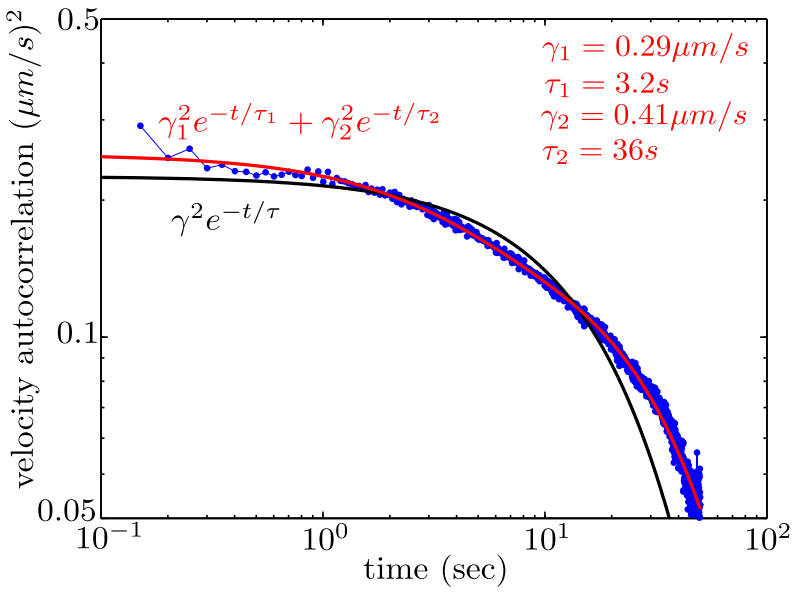

FIG. S12: Velocity autocorrelation function C_v (blue) for pooled tracks from 93 HL60 cells. Single exponential fit is shown in black and double exponential in red.

S9. SELECTION OF $n_{\max}$ FOR ANALYZING LYSOSOME MOTION

To determine the appropriate wavelet spans for the BNEW analysis of lysosome motion in neutrophils, it is necessary to first calculate an approximation of the drift velocity magnitude and correlation over time. We pool together lysosome tracks from all 93 cells and calculate the velocity autocorrelation function, defined as

$$C_v(t) = \frac{1}{\Delta^2} \langle [\vec{p}(t' + \Delta) - \vec{p}(t')] \cdot [\vec{p}(t' + t + \Delta) - \vec{p}(t' + t)] \rangle \tag{S36}$$

where the average is done over all tracks and all time points t'. The velocity autocorrelation contains components from the drift velocity, the stochastic motion and the localization error. However, if we assume that the stochastic particle motion is diffusive, then this should contribute only to the $t = 0$ correlation timepoint and if the localization error is uncorrelated in time, then it should contribute to the $t = 0$ and $t = \Delta$ timepoints only. We thus consider the autocorrelation function for $t \geq 2\Delta$ only to focus specifically on the drift velocity.

This autocorrelation is not well fit by a single exponential, but can be approximately fit to a double exponential decay (Fig. S12). We use this approximate functional form to select the optimal maximal wavelet span $n_{\max}$ to use in the BNEW analysis. Specifically, we approximate the drift as the composition of two independent persistent random walks with correlation times $\tau_1 = 1.1$ sec and $\tau_2 = 25$ sec and magnitudes $\gamma_1 = 0.49\mu m/s$ and $\gamma_2 = 0.58\mu m/s$, respectively. The error in the fitted parameters can then be calculated using a generalization of Eq. S27,

$$\begin{aligned} \mathrm{cov}\left(\eta_l^{(m_1)}, \eta_{l+q}^{(m_2)}\right) =& (\gamma_1\Delta)^4 H^{(u,1)}_{m_1,m_2} + (\gamma_2\Delta)^4 H^{(u,2)}_{m_1,m_2} + (2D\Delta)^2 H^{(v)}_{m_1,m_2} + \epsilon^2 H^{(\xi)}_{m_1,m_2} \\ &+2\Delta^2 \left[\gamma_1^2 F^{(u,1)}_{m_1,m_2} + \gamma_2^2 F^{(u,2)}_{m_1,m_2}\right] \left[2D\Delta F^{(v)}_{m_1,m_2} + \epsilon^2 F^{(\xi)}_{m_1,m_2}\right] \\ &+4D\epsilon^2\Delta F^{(v)}_{m_1,m_2} F^{(\xi)}_{m_1,m_2} + 2\gamma_1^2\gamma_2^2\Delta^4 F^{(u,1)}_{m_1,m_2} F^{(u,2)}_{m_1,m_2}, \end{aligned} \tag{S37}$$

where $\mathbf{H}^{(u,1)}, \mathbf{H}^{(u,2)}$ refer to the fourth order correlation matrices (Eq. S28) and $\mathbf{F}^{(u,1)}, \mathbf{F}^{(u,2)}$ to the

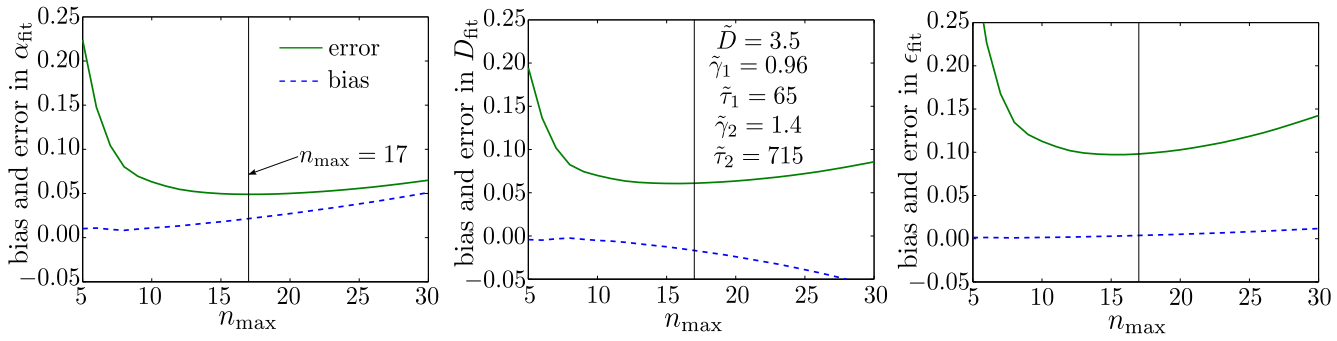

FIG. S13: Analytically approximated errors in estimated fit parameters with the BNEW method, assuming drift velocity composed of two independent persistent random walks with dimensionless correlation times $\tilde{\tau}_1, \tilde{\tau}_2$ and magnitudes $\tilde{\gamma}_1, \tilde{\gamma}_2$, respectively. Stochastic motion is assumed diffusive with dimensionless diffusion constant $\tilde{D}$. Time units are non-dimensionalized by the time step $\Delta = 0.05s$ and length units by the localization error $\epsilon = 0.015\mu m$. The drift velocity parameters are selected based on the pooled velocity autocorrelation function for all cells (Fig. S12), and the diffusion constant and localization error based on BNEW analysis results with SG-3 wavelets of span $2 \leq n \leq 17$ and time separations $1 \leq k \leq \lfloor 0.74n \rfloor$ (Fig. 5). Bias and error in $\tilde{D}_{\rm fit}$ are shown as fractions of $\tilde{D}$. Bias and error in $\alpha_{\rm fit}, \tilde{\epsilon}_{\rm fit}$ are shown in dimensionless units. Error calculations are done for a total of 391 tracks of length 118 time points each.

second order correlation matrices (Eq. S30), based on τ_1 and τ_2, respectively.

The analytically calculated errors in the fitted parameters for this approximate double-exponential drift velocity are plotted in Fig. S13 as a function of the maximal wavelet span $n_{\rm max}$. For this analysis, we assume 391 tracks of length 118 time points each, the mean values for the population of HL60 cells.

We find that the minimum error in estimating the viscoelastic scaling α occurs for $n_{\rm max} = 17$, which we use for the analysis of the experimental data. The dimensionless values of the diffusion coefficient ($\tilde{D} \approx 3.5$) and drift velocities ($\tilde{\gamma}_1 \approx 1, \tilde{\gamma}_2 \approx 1.4$) used to select the optimal $n_{\rm max}$ were taken from the BNEW analysis statistics of the population of HL60 cells (Fig. 5). The choice of wavelet span used for the analysis is thus self-consistent with the parameters obtained from the analysis itself.

S10. QUANTIFYING LOCALIZATION ERROR WITH A FIXED CELL

We obtain an independent measurement of the localization error inherent in our imaging protocol by tracking labeled lysosome particles in several HL60 cells fixed with formaldehyde/glutaraldehyde (see Experimental Methods). The mean squared displacement of the particles is approximately constant with time for short times (Fig. S14a), and the distribution of individual step sizes is shown in Fig. S14b. The localization error is estimated from the root mean squared displacement over a single time step,

$$\epsilon = \sqrt{\left\langle \left| \vec{p}(\Delta) - \vec{p}(0) \right|^2 \right\rangle / 4} \approx 0.014\mu m \tag{S38}$$

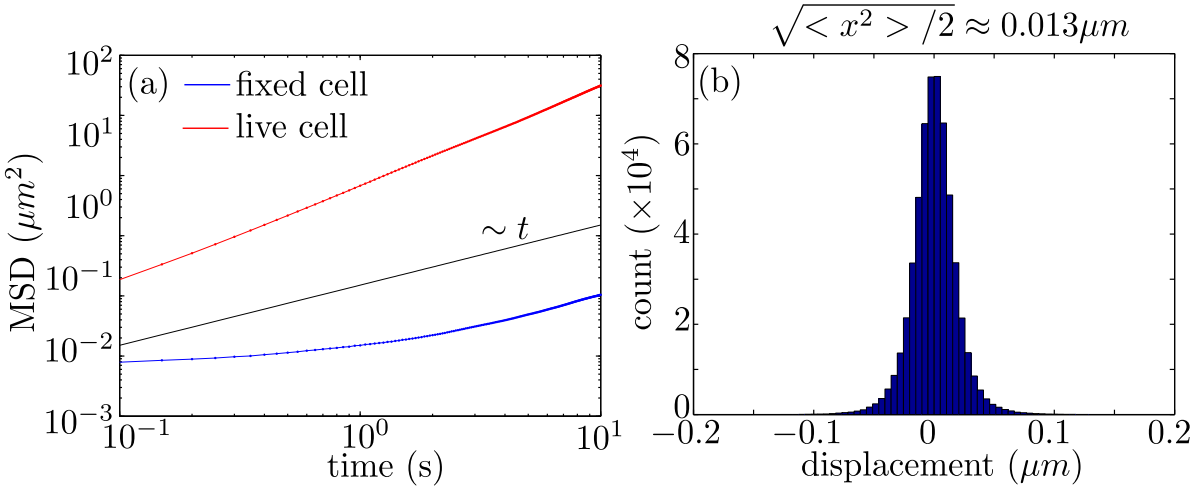

FIG. S14: Particle trajectory analysis for fixed cells (statistics from 11 cells total). (a) Mean squared displacement of lysosomes in fixed HL60 cells (blue) and a live cell (red, cell shown in Fig. 4). Linear scaling indicated with black line. (b) Histogram of step sizes for lysosome displacement in fixed cells, along a single dimension, over one time step ($\Delta = 0.05s$).

[1] K. Chen, B. Wang, J. Guan, and S. Granick, ACS Nano **7**, 8634 (2013).
[2] A. Savitzky and M. J. Golay, Anal Chem **36**, 1627 (1964).
[3] R. W. Schafer, IEEE Signal Proc Mag **28**, 111 (2011).
[4] W. Deng and E. Barkai, Phys Rev E **79**, 011112 (2009).
[5] D. P. Kroese and Z. I. Botev, arXiv preprint arXiv:1308.0399 (2013).
[6] S. C. Weber, J. A. Theriot, and A. J. Spakowitz, Phys Rev E **82**, 011913 (2010).
[7] P. Turchin, *Quantitative analysis of movement: measuring and modeling population redistribution in animals and plants*, vol. 1 (Sinauer Associates Sunderland, 1998).
[8] D. Selmeczi, S. Mosler, P. H. Hagedorn, N. B. Larsen, and H. Flyvbjerg, Biophys J **89**, 912 (2005).
[9] C. Bouchiat, M. Wang, J.-F. Allemand, T. Strick, S. Block, and V. Croquette, Biophys J **76**, 409 (1999).
[10] H. Yamakawa, *Helical wormlike chains in polymer solutions* (Springer Science & Business Media, 2012).
[11] T. Kariya and H. Kurata, *Generalized least squares* (John Wiley & Sons, 2004).
[12] X. Michalet, Phys Rev E **82**, 041914 (2010).